Key Points:
- X-ray diffraction data and equations of state of bcc- and hcp- $Fe_{0.91}Ni_{0.09}$ and $Fe_{0.8}Ni_{0.1}Si_{0.1}$ are reported at 300 K up to ~170 GPa
- Thermal equations of state are combined with seismic observations and error propagation to place constraints on the inner core composition
- The hcp axial ratios of $Fe_{0.91}Ni_{0.09}$ and $Fe_{0.8}Ni_{0.1}Si_{0.1}$ at 300 K and their relation to P wave anisotropy are investigated

Supporting Information:
- Supporting Information S1
- Table S1
- Table S2
- Table S3
- Table S4

Correspondence to:
R. A. Morrison and J. M. Jackson,
rmorrison@caltech.edu;
jackson@gps.caltech.edu

Equations of State and Anisotropy of Fe-Ni-Si Alloys

Rachel A. Morrison[1] [iD], Jennifer M. Jackson[1] [iD], Wolfgang Sturhahn[1] [iD], Dongzhou Zhang[2,3] [iD], and Eran Greenberg[4] [iD]

[1] Seismological Laboratory, California Institute of Technology, Pasadena, CA, USA, [2] Hawaii Institute of Geophysics and Planetology, University of Hawaii at Manoa, Honolulu, HI, USA, [3] GSECARS, University of Chicago, Argonne, IL, USA, [4] Center for Advanced Radiation Sources, University of Chicago, Chicago, IL, USA

Abstract We present powder X-ray diffraction data on body centered cubic (bcc)- and hexagonal close packed (hcp)-structured $Fe_{0.91}Ni_{0.09}$ and $Fe_{0.8}Ni_{0.1}Si_{0.1}$ at 300 K up to 167 and 175 GPa, respectively. The alloys were loaded with tungsten powder as a pressure calibrant and helium as a pressure transmitting medium into diamond anvil cells, and their equations of state and axial ratios were measured with high statistical quality. These equations of state are combined with thermal parameters from previous reports to improve the extrapolation of the density, adiabatic bulk modulus, and bulk sound speed to the pressures and temperatures of Earth's inner core. We propagate uncertainties and place constraints on the composition of Earth's inner core by combining these results with available data on light-element alloys of iron and seismic observations. For example, the addition of 4.3 to 5.3 wt% silicon to $Fe_{0.95}Ni_{0.05}$ alone can explain geophysical observations of the inner core boundary, as can up to 7.5 wt% sulfur with negligible amounts of silicon and oxygen. Our findings favor an inner core with less than ~2 wt% oxygen and less than 1 wt% carbon, although uncertainties in electronic and anharmonic contributions to the equations of state may shift these values. The compositional space widens toward the center of the Earth, considering inner core seismic gradients. We demonstrate that hcp-$Fe_{0.91}Ni_{0.09}$ and hcp-$Fe_{0.8}Ni_{0.1}Si_{0.1}$ have measurably greater c/a axial ratios than those of hcp-Fe over the measured pressure range. We further investigate the relationship between the axial ratios, their pressure derivatives, and elastic anisotropy of hcp-structured materials.

1. Introduction

Earth models, such as the Preliminary Reference Earth Model (Dziewonski & Anderson, 1981) and AK135-F (Kennett et al., 1995), provide one-dimensional radial models of the compressional, shear, and bulk sound velocities down to the center of Earth. Combined with a model for the density distribution within Earth, these models provide the adiabatic bulk and shear moduli along this 1-D profile. Cosmochemical studies suggest that the Earth is composed primarily of iron alloyed with approximately 5 wt% nickel (Allègre et al., 1995; McDonough, 2003). The presence of some amount of light elements (e.g., Si, O, S, C, and H) inside the core has been suggested based upon the properties of pure iron and their deviation from these seismically inferred values (e.g., Allègre et al., 1995; Campbell, 2016; Hirose et al., 2013; Li & Fei, 2014; McDonough, 2003; Ohtani, 2013).

Regional seismic studies have provided additional insight to this remote region of the planet, suggesting evidence for an anisotropic inner core (e.g., Attanayake et al., 2014; Lythgoe et al., 2014, and for a recent review, see Deuss, 2014). Various origins of this anisotropy have been put forth, including the preferred alignment of elastically anisotropic crystallites of iron alloys. Studies have suggested that the elastic anisotropy of a material with a hexagonal close packed (hcp) crystal structure is related to the value of its c/a axial ratio (Asker et al., 2009; Fischer & Campbell, 2015; Gannarelli et al., 2005; Ono et al., 2010; Sha & Cohen, 2006).

The equation of state (EOS) and c/a axial ratio of pure hcp-iron have been well constrained by a powder X-ray diffraction study at 300 K, which used tungsten as a pressure marker and helium as a pressure medium (Dewaele et al., 2006). Helium is considered to provide more uniform stress conditions inside the sample chamber compared to other commonly selected pressure media, especially under extreme conditions (Klotz et al., 2009; Zarochentsev et al., 2004). While an iron-nickel diamond anvil cell (DAC) study up to 255 GPa suggested the pressure-volume relation of iron is indistinguishable from that of iron alloyed with 20 at% nickel (Mao et al., 1990), a systematic study evaluating the effect of alloying iron with nickel in a helium pressure

medium has not yet been conducted. The Mao et al. (1990) study was conducted without the use of a pressure medium and with the platinum pressure calibrant of Holmes et al. (1989). Subsequent EOS experiments have predominantly neglected nickel and focused on iron alloyed with various light elements (Hirose et al., 2013; Poirier, 1994). However, the presence of nonhydrostatic stress conditions could blur such compositional effects, as it is known that the lattice parameters and resulting unit cell volumes can be highly sensitive to stress conditions (e.g., Zhao & Ross, 2015). The stress conditions inside Earth's core are thought to be hydrostatic, so achieving experimental conditions that are as close to hydrostatic as possible is critical. There is also little consensus on the values and trends of c/a axial ratios of hcp-iron alloys at ambient temperature (e.g., Asker et al., 2009; Fischer & Campbell, 2015; Gannarelli et al., 2005; Ono et al., 2010; Sha & Cohen, 2006). Determination of these quantities for a suite of iron alloys under low deviatoric stress conditions can provide important constraints on compositional effects.

In this study, we present high-precision pressure-volume data for $Fe_{0.91}Ni_{0.09}$ and $Fe_{0.8}Ni_{0.1}Si_{0.1}$ using powder X-ray diffraction at 300 K up to 167 and 175 GPa, respectively. By using tungsten powder as pressure calibrant and helium as a pressure transmitting medium, we minimize error in determination of compositional effects due to pressure calibration and nonhydrostatic stresses. The results are a suite of high fidelity data sets fit with equations of state, as well as precise c/a axial ratios for the hcp alloys. By systematically comparing our findings to those of pure iron (Dewaele et al., 2006), we constrain the effect of nickel and silicon on the density, bulk modulus, and bulk sound speed of iron alloys, which is a critical step in constraining the inner core's composition. We find that for iron alloys, constraining the EOS at 300 K significantly reduces the uncertainty of high-temperature equations of state extrapolated to inner core conditions. After extrapolating our hcp-$Fe_{0.91}Ni_{0.09}$ and hcp-$Fe_{0.8}Ni_{0.1}Si_{0.1}$ equations of state to inner core conditions, we estimate the allowable inner core composition in Fe-Ni-Si composition space and then extrapolate to the Fe-Ni-Si-O-C-S composition space. From our X-ray diffraction data, we also obtain an unprecedented constraint on the effect of nickel and silicon on the axial ratio of these iron alloys, and we investigate the relationship between the axial ratio, its pressure derivative, and anisotropy of hcp-structured materials.

2. Experimental Methods

The samples were synthesized from individual pieces of Ni, Si, and 95%-enriched ^{57}Fe to produce iron containing $\sim$10 wt% nickel and iron containing $\sim$10 wt% nickel and $\sim$5 wt% silicon. The Fe, Ni, and Si pieces were arc melted in an argon atmosphere and then cold rolled to $\sim$10 μm. Sample compositions were confirmed with scanning electron microscopy (SEM) measurements to be $Fe_{0.91(1)}Ni_{0.09(1)}$ and $Fe_{0.80(1)}Ni_{0.10(1)}Si_{0.10(1)}$, and sample homogeneity was observed at a scale of 1 μm. The unit cell volume is insensitive to the ^{57}Fe enrichment of our samples. We remove the effect of the enrichment of our sample by using the natural abundance of iron to compute the density.

To achieve high pressures, the iron alloys were cut to a range of lateral dimensions and placed in the center of the sample chamber of symmetric DACs with diamond culet diameters of 100 or 250 μm and bevels extending to 300 μm. Rhenium gaskets were used to maintain sample-chamber integrity. Each gasket was indented to a thickness of $20-40$ μm and then drilled with a 65-130 μm diameter hole using an electron discharge machine. A cubic boron nitride seat on the downstream side of the DAC maximized the accessible 2θ range for X-ray diffraction measurements. We placed tungsten powder proximal to the sample in the sample chamber to act as a pressure calibrant. Tungsten was selected as a pressure calibrant for its high X-ray scattering coefficient, its well-known EOS (e.g., Dewaele et al., 2004; Dorogokupets & Oganov, 2006), and its use as a pressure calibrant in a study on pure iron (Dewaele et al., 2006). The sample chamber was filled with compressed helium at 25,000 PSI as a pressure transmitting medium with the gas loading facility located at Caltech. Helium's remarkably low shear modulus (Zarochentsev et al., 2004) enables the measurement of highly accurate data, including the c/a axial ratios of the hcp-structured phases. The X-ray powder diffraction study on iron by Dewaele et al. (2006) also used helium as a pressure medium. Thus, the similarity in sample environments permits a more precise comparison of the iron alloys investigated in this study to those of iron.

Powder X-ray diffraction experiments were conducted at GSECARS' beamlines 13-BM-C and 13-ID-D at the Advanced Photon Source (APS) near Chicago and at beamline 12.2.2 at the Advanced Light Source in Berkeley. Each beamline delivered slightly different characteristics of the X-rays for the $Fe_{0.91}Ni_{0.09}$ and $Fe_{0.8}Ni_{0.1}Si_{0.1}$ experimental runs (hereafter referred to as FeNi-Run#1, FeNi-Run#2, FeNi-Run#3, FeNiSi-Run#1, and FeNiSi-Run#2). Specifically, a beam size of $\sim$15 $\times$ 15 μm^2 full width at half maximum (FWHM) and an energy of 28.57 keV was used at APS sector 13-BM-C for FeNi-Run#1. A beam size of $\sim$20 $\times$ 20 μm^2 FWHM
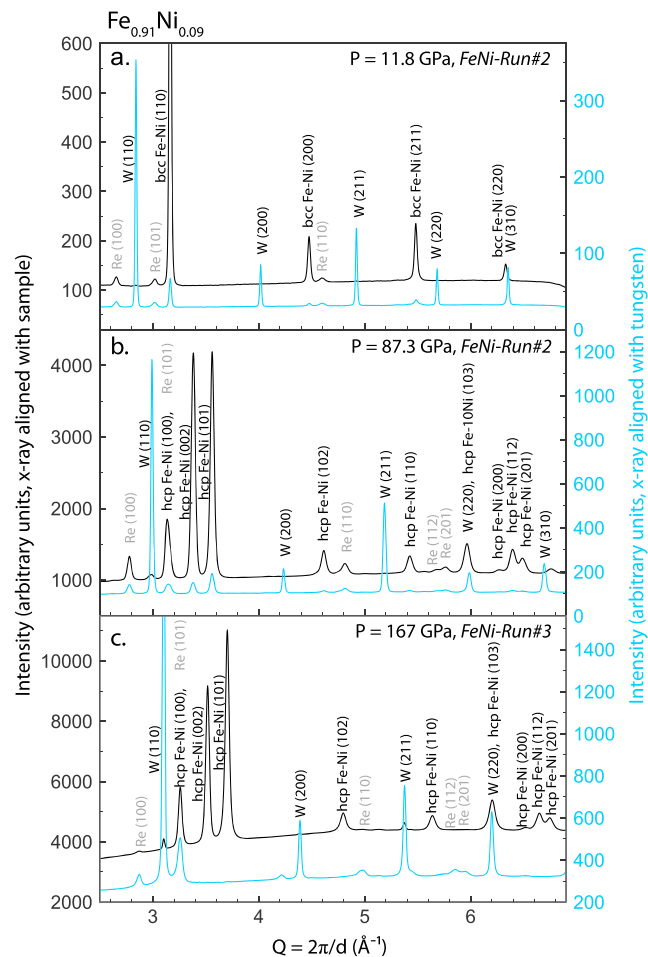
Figure 1. X-ray diffraction patterns at 300 K for (a) bcc-$Fe_{0.91}Ni_{0.09}$ at 11.8 GPa, (b) hcp-$Fe_{0.91}Ni_{0.09}$ at 87.3 GPa, and (c) hcp-$Fe_{0.91}Ni_{0.09}$ at 167 GPa. Patterns are plotted against Q ($= 2\pi/d$) instead of 2θ to remove the dependency on wavelength. Patterns were collected with the sample (black curves, left y axis) and with the tungsten powder (blue curves, right y axis) aligned with the X-ray focus. Patterns are plotted before background subtraction.

and energies of 30 and 35 keV were used at beamline 12.2.2 at the Advanced Light Source for FeNiSi-Run#1 and for FeNi-Run#2. A beam size of ~3 × 3 μm^2 FWHM and an energy of 37.08 keV was used at APS sector 13-ID-D for FeNi-Run#3 and FeNiSi-Run#2. Pressure was increased manually off-line for FeNi-Run#1, FeNi-Run#2, and FeNiSi-Run#1. For FeNiSi-Run#2 and FeNi-Run#3 at APS sector 13-ID-D, pressure was increased in situ using a membrane DAC (Sinogeikin et al., 2015). The standard LaB_6 was used to calibrate X-ray diffraction images for all runs except FeNi-Run#2, when the calibrant CeO_2 was used. Experimental conditions for each run are summarized in Table S5 in the supporting information.

X-ray diffraction images were integrated with the software Dioptas (Prescher & Prakapenka, 2015). Example X-ray diffraction patterns for body centered cubic (bcc)- and hcp-$Fe_{0.91}Ni_{0.09}$ and bcc- and hcp-$Fe_{0.8}Ni_{0.1}Si_{0.1}$ are shown in Figures 1 and 2, respectively. The structural phase transition from bcc to hcp was identified by the appearance of peaks associated with the hcp phase and the disappearance of peaks associated with the bcc phase. Lattice parameters of the iron alloys and of the tungsten powder were determined using full-profile Pawley refinement and were consistent with those obtained using the Pawley refinement approach in the GSAS-II software package (Toby & Von Dreele, 2013). The sample and tungsten unit cell volumes were calculated from the refined lattice parameters a for bcc phases and a and c for hcp phases.

The tungsten EOS from Dorogokupets and Oganov (2006) was used to determine sample pressure. This EOS has been calibrated with modern shock wave, X-ray, and ultrasonic measurements collectively. Use of this
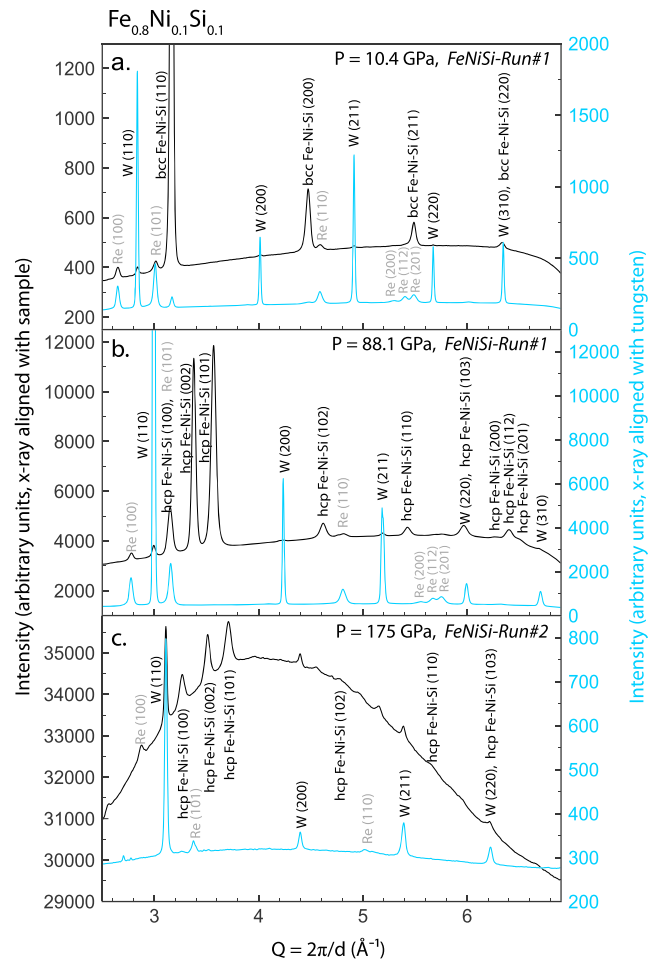
Figure 2. X-ray diffraction patterns at 300 K for (a) bcc-$Fe_{0.8}Ni_{0.1}Si_{0.1}$ at 10.4 GPa, (b) hcp-$Fe_{0.8}Ni_{0.1}Si_{0.1}$ at 88.1 GPa, and (c) hcp-$Fe_{0.8}Ni_{0.1}Si_{0.1}$ at 175 GPa. Patterns are plotted against Q (= $2\pi/d$) instead of against 2θ to remove the dependency on wavelength. Patterns were collected with the sample (black curves, left y axis) and with the tungsten powder (blue curves, right y axis) aligned with the X-ray focus. Patterns are plotted before background subtraction.

pressure calibration allows for a systematic comparison of our $Fe_{0.91}Ni_{0.09}$ and $Fe_{0.8}Ni_{0.1}Si_{0.1}$ studies with the study by Dewaele et al. (2006) on pure iron, which also used the Dorogokupets and Oganov (2006) tungsten pressure calibration.

2.1. Lattice Parameter Error Analysis

The lattice parameter uncertainties for $Fe_{0.91}Ni_{0.09}$, $Fe_{0.8}Ni_{0.1}Si_{0.1}$, and tungsten were obtained from the refinement of each X-ray diffraction pattern. However, full-profile refinement methods are known to significantly underestimate lattice parameter uncertainties (Angel, 2000). We estimate the lattice parameter uncertainty with scaling factors k, where the lattice parameter uncertainty σ obtained from refinement of an individual pattern for a given phase is replaced by $k\sigma$ (Angel, 2000). We apply the same scaling parameter k to all data within a given phase. To estimate the uncertainty scaling parameters for each phase of a particular composition (bcc Fe-alloys, hcp Fe-alloys, and bcc-tungsten), we used two general principles. First, when fitting an EOS to experimental pressure-volume data from a single run, the reduced goodness of fit (χ^2) should be close to 1. The uncertainty on each data point should not be smaller than is justified by the scatter of the data, assuming the model to fit the data (i.e., the EOS) is reasonable. Second, when an EOS is fit to data combined from multiple runs, the χ^2 should be approximately 1, because a better estimate of uncertainty is obtained from multiple repetitions of the same experiment than is obtained from a single experiment; thus, when an EOS is fit to data combined from multiple runs, the reduced χ^2 should be approximately 1. As a result of this uncertainty estimation, the reduced goodness of fit (χ^2) is ~1 for each of our EOS fits.

Table 1
Equation of State Fitting Parameters

Reference	Phase	Composition	V_0 (Å^3)	K_0 (GPa)	K'_0	P range (GPa)	P medium	P gauge	EOS
This study	bcc	Fe$_{0.91}$Ni$_{0.09}$	23.635(6)	146.7(30)	6.42(60)	0–15.2	He	W	Vinet
			23.635(6)	146.8(31)	6.39(64)				BM3
This study	bcc	Fe$_{0.8}$Ni$_{0.1}$Si$_{0.1}$	23.385(9)	155.6(74)	5.7(12)	0–21.6	He	W	Vinet
			23.384(9)	155.9(75)	5.6(13)				BM3
This study	hcp	Fe$_{0.91}$Ni$_{0.09}$	22.505(42)	157.5(39)	5.61(10)	14.6–167	He	W	Vinet
			22.436(40)	167.4(40)	5.07(10)				BM3
This study	hcp	Fe$_{0.8}$Ni$_{0.1}$Si$_{0.1}$	22.952(72)	125.2(46)	6.38(12)	21.6–175	He	W	Vinet
			22.837(71)	135.8(52)	5.84(14)				BM3
Dewaele et al. (2006)	bcc	Fe (Our fit)[a]	23.524(18)	168.1(83)	4.7(13)	0–14.6	He	W, ruby	Vinet
Dewaele et al. (2006)	hcp	Fe	22.428(98)	163.4(79)	5.38(16)	17–197	He	W, ruby	Vinet
			22.468(24)	165 (fixed)	4.97(4)				BM3
		(Refit)[b]	22.425(54)	162.9(45)	5.40(9)				*Vinet*

[a]As Dewaele et al. (2006) report no bcc-iron equation of state (EOS), we fit a Vinet EOS to their reported bcc-iron data. [b]We refit hcp-iron data (Dewaele et al., 2006) with a Vinet EOS to obtain fit parameter correlations. Our refit is consistent with the original Vinet EOS fit by Dewaele et al. (2006).

Proper propagation of uncertainty from a particular pressure calibrant requires knowledge of the corresponding error correlation matrix of the data used to create the pressure scale. As the error correlation matrix for the Dorogokupets and Oganov (2006) tungsten EOS is not available, the pressure calibration is treated as given. Nevertheless, the uncertainty for the Dorogokupets and Oganov (2006) tungsten pressure standard agrees with aluminum, gold, copper, platinum, and tantalum pressure standards within 2 GPa at 160 GPa and 300 K (Dorogokupets & Oganov, 2006), which is of comparable magnitude with our reported pressure uncertainty (see Tables S1–S4 in the supporting information).

3. X-Ray Diffraction Results

3.1. Fe$_{0.91}$Ni$_{0.09}$

X-ray diffraction images were collected from pressures ranging from 0 to 167 GPa over three separate experimental runs (FeNi-Run#1, FeNi-Run#2, and FeNi-Run#3) at 300 K. Example X-ray diffraction patterns for Fe$_{0.91}$Ni$_{0.09}$ are shown in Figure 1. Fe$_{0.91}$Ni$_{0.09}$ is stable in the bcc structure at ambient conditions, and a phase transition to the hcp structure was constrained to pressures between 12.5 and 17.2 GPa. Fe$_{0.91}$Ni$_{0.09}$ is thought to be stable in the hcp phase in the Earth's inner core (Tateno et al., 2012). Minor texturing was observed in the X-ray diffraction images at all pressures due to cold rolling of the samples during synthesis. However, the sample X-ray diffraction peak 2θ positions did not vary radially around the X-ray diffraction image, indicating the minor texturing of the sample had a negligible effect on the determined peak positions. The bcc-Fe$_{0.91}$Ni$_{0.09}$ lattice parameters were determined from the d-spacings of the following four reflections: 110, 200, 211, and 220. The hcp-Fe$_{0.91}$Ni$_{0.09}$ lattice parameters were determined from the d-spacings of the following nine reflections: 100, 002, 101, 102, 110, 103, 200, 112, and 201. The bcc-tungsten lattice parameters were determined from the d-spacings of the following five reflections: 110, 200, 211, 220, and 310. Lattice parameters, volumes, and pressures are given in Tables S1 and S2 in the supporting information.

3.2. Fe$_{0.8}$Ni$_{0.1}$Si$_{0.1}$

X-ray diffraction images were collected from pressures ranging from 0 to 175 GPa over two separate experimental runs (FeNiSi-Run#1 and FeNiSi-Run#2) at 300 K. Example X-ray diffraction patterns for Fe$_{0.8}$Ni$_{0.1}$Si$_{0.1}$ are shown in Figure 2. Fe$_{0.8}$Ni$_{0.1}$Si$_{0.1}$ is also stable in the bcc structure at ambient conditions and undergoes a phase transition to the hcp structure at a higher pressure than Fe$_{0.91}$Ni$_{0.09}$. The bcc-hcp phase transition for Fe$_{0.8}$Ni$_{0.1}$Si$_{0.1}$ was constrained to be above 18.7 GPa and below 24.5 GPa, demonstrating that 10 at% Si stabilizes the bcc phase by about 6 GPa. Similar to the Fe$_{0.91}$Ni$_{0.09}$ samples, minor texturing was observed in the Fe$_{0.8}$Ni$_{0.1}$Si$_{0.1}$ samples at all pressures due to cold rolling. As in the case of the Fe$_{0.91}$Ni$_{0.09}$ samples, the sample X-ray diffraction peak 2θ positions did not vary radially around the X-ray diffraction image. The higher background in FeNiSi-Run#2 at higher pressures is likely due to a combination of Compton scattering from thicker diamond anvils (~2.2 mm compared with ~2.0 mm) and minor sample thickness variations at higher
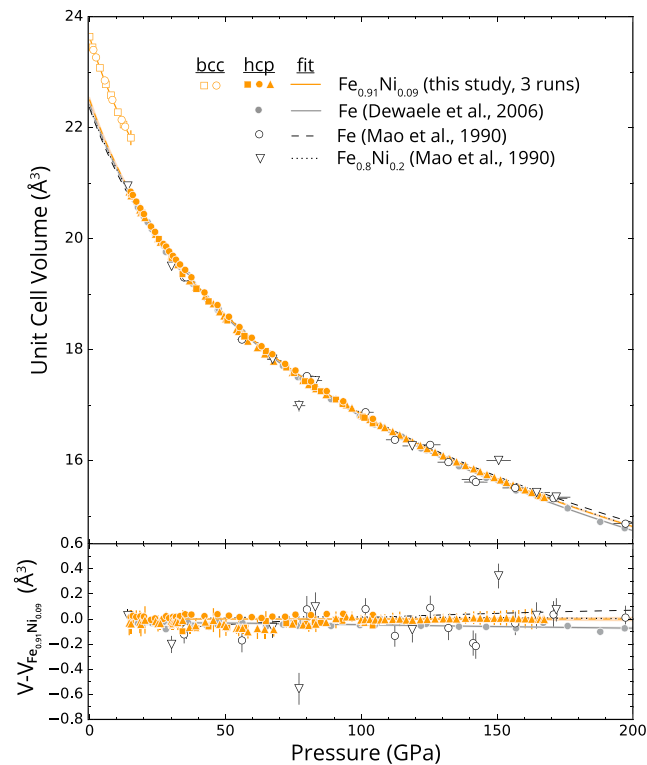
Figure 3. Volume-pressure relation for data and equation of state fits for bcc- and hcp-$Fe_{0.91}Ni_{0.09}$, where the symbols refer to different experimental runs. We compare to hcp-Fe (Dewaele et al., 2006), hcp-Fe (H. K. Mao et al., 1990), and hcp-$Fe_{0.8}Ni_{0.2}$ (H. K. Mao et al., 1990). In the bottom panel, the hcp-$Fe_{0.91}Ni_{0.09}$ equation of state (this study) is subtracted from all hcp data and fits.

pressures. For consistency, the bcc- and hcp-$Fe_{0.8}Ni_{0.1}Si_{0.1}$ lattice parameters and the bcc-tungsten lattice parameters were constrained using the same set of reflections as for the $Fe_{0.91}Ni_{0.09}$ data in this study. Lattice parameters, volumes, and pressures are given in Tables S3 and S4 in the supporting information.

4. Equations of State

We used the open-source software package MINUTI version 2.0.0 (Sturhahn, 2017) to fit both Vinet and third-order Birch-Murnaghan EOSs to the 300 K bcc- and hcp-$Fe_{0.91}Ni_{0.09}$ and $Fe_{0.8}Ni_{0.1}Si_{0.1}$ data. For each phase of each composition, we combine all runs into a single data set and fit three parameters: ambient volume V_0, ambient isothermal bulk modulus K_{T0}, and the ambient pressure derivative of the bulk modulus K'_{T0}. No parameters were fixed in these EOS fits, and no priors based on other studies were applied. The resulting EOS parameters are given in Table 1, and the correlations between model parameters are given in Tables S6 and S7 in the supporting information.

4.1. $Fe_{0.91}Ni_{0.09}$

We present the bcc- and hcp-$Fe_{0.91}Ni_{0.09}$ pressure-volume data and Vinet EOS fits in Figure 3. We compare to the hcp-Fe x-ray diffraction study up to 205 GPa at 300 K, which was conducted with a helium pressure medium and a tungsten pressure calibrant and fit with a Vinet EOS (Dewaele et al., 2006). We also compare to the hcp-Fe and hcp-$Fe_{0.8}Ni_{0.2}$ X-ray diffraction studies up to 300.6 and 255.0 GPa, respectively, at 300 K, which were conducted with no pressure medium and a platinum pressure calibrant and fit with third-order Birch-Murnaghan EOSs (Mao et al., 1990). In the lower panel of Figure 3, the hcp-$Fe_{0.91}Ni_{0.09}$ EOS from this study was subtracted from all hcp data and fits to elucidate the difference between each EOS. When plotting uncertainty on data in the lower panel, we employ the effective variance method, whereby the uncertainty in pressure is projected into an effective contribution to volume using error propagation. This allows us to effectively one-dimensionalize the plot to more easily distinguish between equations of state. Note that a pressure medium dramatically improves the statistical quality of the data. Although uncertainties for the pressure-volume data were not published in Dewaele et al. (2006) and are thus not shown in Figure 3,
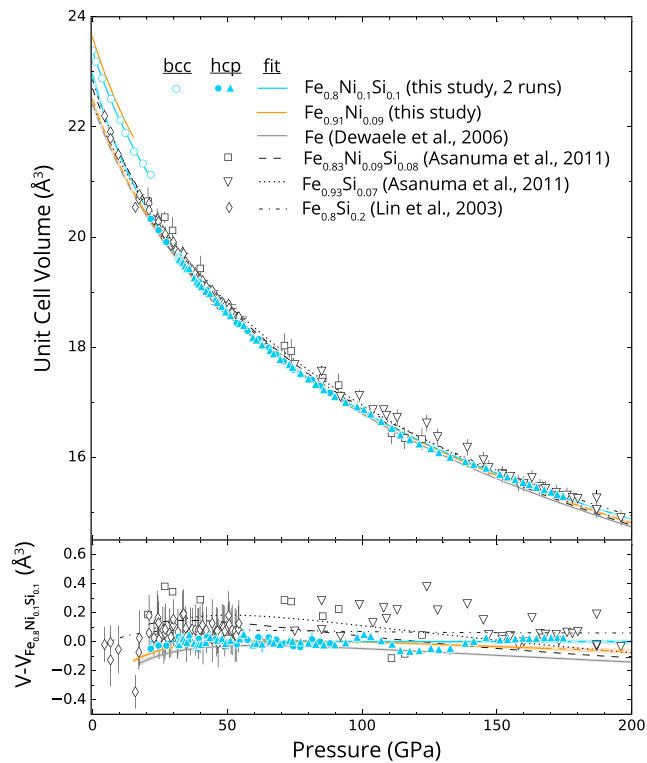
Figure 4. Volume-pressure relation for data and equation of state fits for bcc- and hcp-$Fe_{0.8}Ni_{0.1}Si_{0.1}$, where the symbols refer to different experimental runs. We compare to hcp-$Fe_{0.83}Ni_{0.09}Si_{0.08}$ (Asanuma et al., 2011), hcp-$Fe_{0.93}Si_{0.07}$ (Asanuma et al., 2011), and hcp-$Fe_{0.85}Si_{0.15}$ (Lin, 2003). For reference, the equations of state for $Fe_{0.91}Ni_{0.09}$ (this study) and Fe (Dewaele et al., 2006) are also plotted. In the bottom panel, the hcp-$Fe_{0.8}Ni_{0.1}Si_{0.1}$ equation of state (this study) is subtracted from all hcp data and fits.

one can see that the volumes of iron and $Fe_{0.91}Ni_{0.09}$ diverge by ∼0.1 Å^3 at ∼150 GPa. Therefore, only with high-precision X-ray diffraction data can such differences, or lack thereof, be resolved (Figures 3–5).

4.2. $Fe_{0.8}Ni_{0.1}Si_{0.1}$

The bcc- and hcp-$Fe_{0.8}Ni_{0.1}Si_{0.1}$ pressure-volume data and Vinet EOS fits are displayed in Figure 4. We compare to the hcp-$Fe_{0.83}Ni_{0.09}Si_{0.08}$ and hcp-$Fe_{0.93}Si_{0.07}$ X-ray diffraction studies up to 374 and 252 GPa, respectively, which were conducted with a NaCl pressure medium and fit with third-order Birch-Murnaghan equations of state (Asanuma et al., 2011). The NaCl pressure medium also served as a pressure calibrant; however, uncertainties on pressure are not published. We also compare to the hcp-$Fe_{0.85}Si_{0.15}$ X-ray diffraction study up to 54.3 GPa, which was conducted in an ethanol-methanol (1:4) pressure medium with a gold pressure calibrant and fit with a third-order Birch-Murnaghan EOS (Lin, 2003). The Lin (2003) $Fe_{0.85}Si_{0.15}$ study collected X-ray diffraction data both on compression and decompression, and the bcc-hcp transition occurs at lower pressures upon decompression. The hcp-$Fe_{0.91}Ni_{0.09}$ Vinet EOS (this study) and the pure iron Vinet EOS (Dewaele et al., 2006) are also plotted for reference. In the lower panel of Figure 4, the hcp-$Fe_{0.8}Ni_{0.1}Si_{0.1}$ EOS from our study was subtracted from all hcp data and EOS fits to elucidate the difference between each EOS. As described above, when plotting the uncertainty on data in the lower panel, we employ the effective variance method to one-dimensionalize the uncertainties. As uncertainties on pressure are not reported in Asanuma et al. (2011), the uncertainty for the Asanuma et al. (2011) data cannot be properly calculated in the lower panel of Figure 4. Note that a helium pressure medium improves the statistical quality of hcp-iron alloy pressure-volume data.

4.3. Comparison of Fe-Ni-Si Alloys

In Figure 5, we compare the fitted equations of state for the three iron alloy studies conducted in a helium pressure transmitting medium: bcc- and hcp-$Fe_{0.91}Ni_{0.09}$ (this study), bcc- and hcp-$Fe_{0.8}Ni_{0.1}Si_{0.1}$ (this study), and hcp-Fe (Dewaele et al., 2006). As Dewaele et al. (2006) do not report an EOS for bcc-Fe, we fit their bcc-Fe pressure-volume data with a Vinet EOS using MINeral physics UTIlities (MINUTI). The resulting EOS parameters
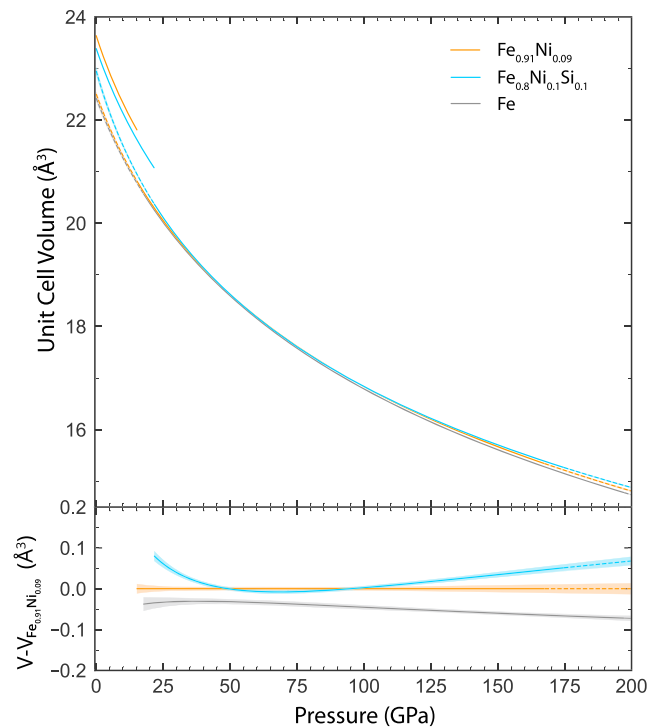
Figure 5. Volume-pressure relation for bcc- and hcp-$Fe_{0.91}Ni_{0.09}$ (this study), bcc- and hcp-$Fe_{0.8}Ni_{0.1}Si_{0.1}$ (this study), and hcp-Fe (Dewaele et al., 2006). All three studies were performed with a helium pressure transmitting medium and used the tungsten pressure calibration by Dorogokupets and Oganov (2006). In the bottom panel, the hcp-$Fe_{0.91}Ni_{0.09}$ EOS (this study) is subtracted from all hcp fits.

and their correlations are given in Table 1 and supporting information Table S6, respectively. The addition of 9 at% Ni to bcc-iron has a measurable effect on the EOS (Figure S1). The further addition of 10 at% Si to bcc-iron decreases the volume and increases the bcc stability field, in agreement with Zhang and Guyot (1999) and Lin (2003). The addition of 9 at% Ni to hcp-iron increases the volume slightly by ∼0.5% at all pressures. The further addition of 10 at% Si results in greater curvature of the pressure-volume relation, thus exhibiting a measurable increase in the pressure derivative of bulk modulus K'_{T0}.

Confidence ellipses provide a valuable assessment tool for comparing model parameters, their uncertainties, and their correlations for EOS fits. In Figure S1 in the supporting information, we plot the K_{T0} and K'_{T0} 68% joint confidence ellipses for our bcc-$Fe_{0.91}Ni_{0.09}$ and bcc-$Fe_{0.8}Ni_{0.1}Si_{0.1}$ studies. We compare these results to our fit of the bcc-Fe data from Dewaele et al. (2006), to the bcc-Fe, bcc-$Fe_{0.95}Ni_{0.05}$, and bcc-$Fe_{0.90}Ni_{0.10}$ equations of state by Takahashi et al. (1968), and to the bcc-Fe and bcc-$Fe_{0.91}Si_{0.09}$ equations of state by Zhang and Guyot (1999). The bcc-$Fe_{0.91}Ni_{0.09}$ confidence ellipse is noticeably smaller than the bcc-$Fe_{0.8}Ni_{0.1}Si_{0.1}$ and bcc-Fe (Dewaele et al., 2006) confidence ellipses due the higher density of data in the bcc-$Fe_{0.91}Ni_{0.09}$ data set.

In panel a of Figure 6, we plot the K_{T0} and K'_{T0} 68% and 95% joint confidence ellipses for our hcp-$Fe_{0.91}Ni_{0.09}$ and $Fe_{0.8}Ni_{0.1}Si_{0.1}$ studies. We compare to the reported EOS parameters from iron alloy X-ray diffraction studies at 300 K described in sections 4.1 and 4.2 (Asanuma et al., 2011; Dewaele et al., 2006; Lin, 2003; H. K. Mao et al., 1990). Confidence ellipses for these studies were not plotted in Figure 6a as none of these studies reported fit parameter correlations. Uncertainties for parameters are plotted as reported. While the K_{T0} and K'_{T0} for hcp-$Fe_{0.91}Ni_{0.09}$ (this study), hcp-Fe (Dewaele et al., 2006), and hcp-Fe and hcp-$Fe_{0.8}Ni_{0.2}$ (H. K. Mao et al., 1990) have similar values, we find that adding 10 at% Ni to Fe slightly decreases K_{T0} and increases K'_{T0}, whereas the opposite conclusions would be reached from the study of H. K. Mao et al. (1990). Note that the effects of Si on the EOS parameters K_{T0} and K'_{T0} of Fe and Fe-Ni alloys were previously poorly constrained and produced contradictory conclusions. We find that adding 10 at% Si to our iron-nickel alloy decreases K_{T0} and increases K'_{T0}. By using the same pressure calibrants and a helium pressure transmitting media, the hcp-$Fe_{0.91}Ni_{0.09}$ and hcp-$Fe_{0.8}Ni_{0.1}Si_{0.1}$ studies paired with the hcp-Fe Dewaele et al. (2006) study provide a systematic constraint on the effect of Si on Fe and Fe-Ni alloys with high statistical quality. Similar plots demonstrating the V_0
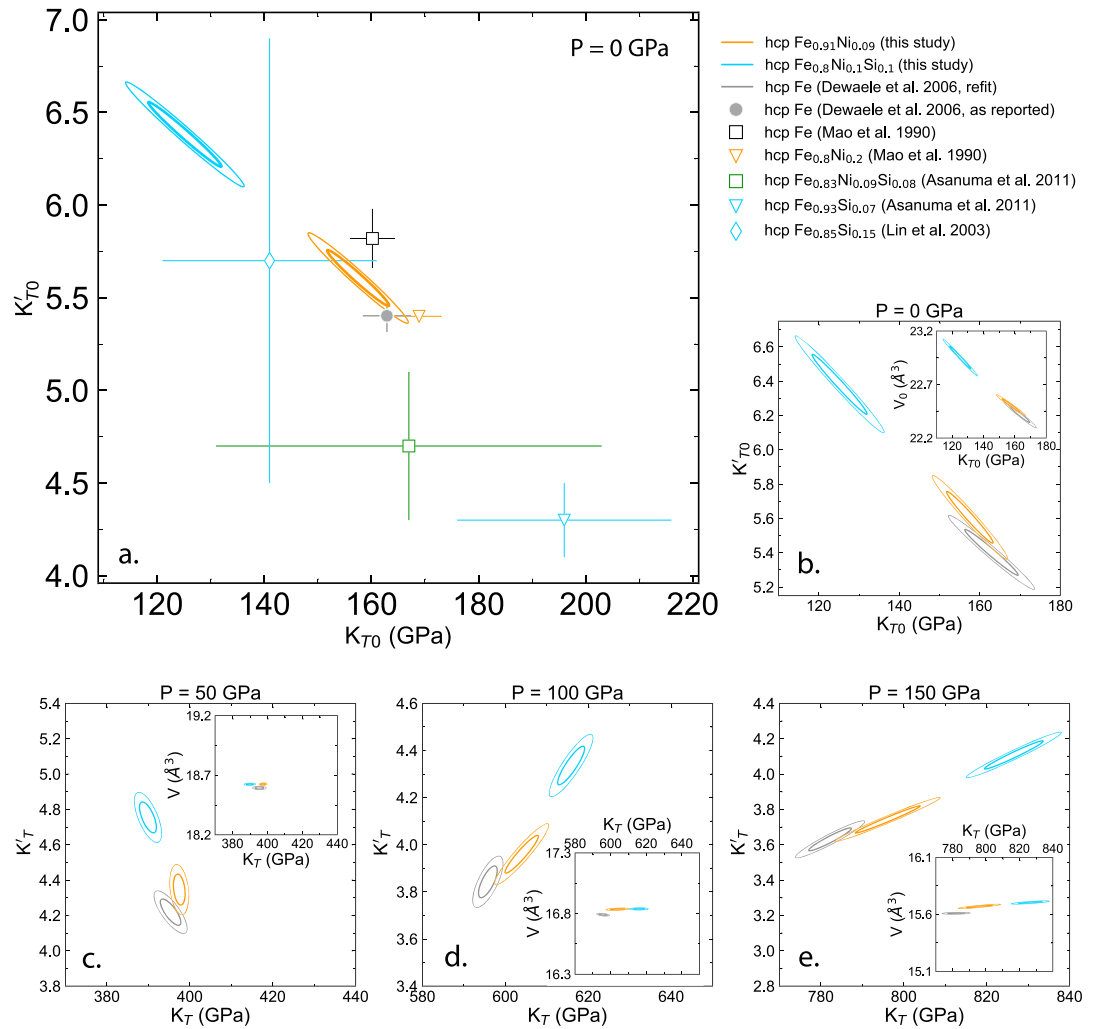
Figure 6. (a) Confidence ellipses for EOS parameters K_{T0} (bulk modulus at 0 GPa) and K'_{T0} (pressure derivative of bulk modulus at 0 GPa) for hcp-$Fe_{0.91}Ni_{0.09}$ and $Fe_{0.8}Ni_{0.1}Si_{0.1}$. Outer thin ellipses represent 95% confidence; inner bold ellipses represent 68% confidence. EOSs without reported correlation matrices are plotted with error bars as reported (see legend). (b–e) Confidence ellipses for K_T and K'_T for hcp-$Fe_{0.91}Ni_{0.09}$, hcp-$Fe_{0.8}Ni_{0.1}Si_{0.1}$, and our refitting of hcp-Fe data (Dewaele et al., 2006) anchored at a variety of pressures. When the EOS is anchored at a pressure outside or near the endpoints of the data range, the EOS parameters are strongly correlated.

and K_{T0} correlation and the V_0 and K'_{T0} correlation for our hcp-$Fe_{0.91}Ni_{0.09}$ and $Fe_{0.8}Ni_{0.1}Si_{0.1}$ studies are shown in Figures S2 and S3 in the supporting information.

The EOS fit parameters are typically defined at 0 GPa for convenience (e.g., V_0, K_{T0}, and K'_{T0}). However, the EOS parameters could just as easily be defined at any other pressure (e.g., $V_{P=50}$, $K_{T,P=50}$, and $K'_{T,P=50}$). As hcp-structure iron alloys are unstable and unquenchable at ambient pressure and temperature, we highlight the importance of comparing various equations of state at pressures where the hcp-phases are stable. For instance, at 0 GPa it is not a surprise that the correlation of parameters is quite large for the hcp phases, especially when compared to the correlation of the parameters of the bcc-phases (supporting information Table S6).

To clearly identify the effects of Ni and Si on the EOS of hcp-iron, we also plot confidence ellipses at 50, 100, and 150 GPa, all of which are within the hcp stability field and within the experimentally measured regions. We plot confidence ellipses from the three studies that were conducted with a helium pressure medium and used the Dorogokupets and Oganov (2006) tungsten pressure calibration: hcp-$Fe_{0.91}Ni_{0.09}$ (this study), hcp-$Fe_{0.8}Ni_{0.1}Si_{0.1}$ (this study), and hcp-Fe (Dewaele et al., 2006). As Dewaele et al. (2006) do not publish EOS parameter correlations, we refit their hcp-Fe data with a Vinet EOS in MINUTI to plot confidence ellipses
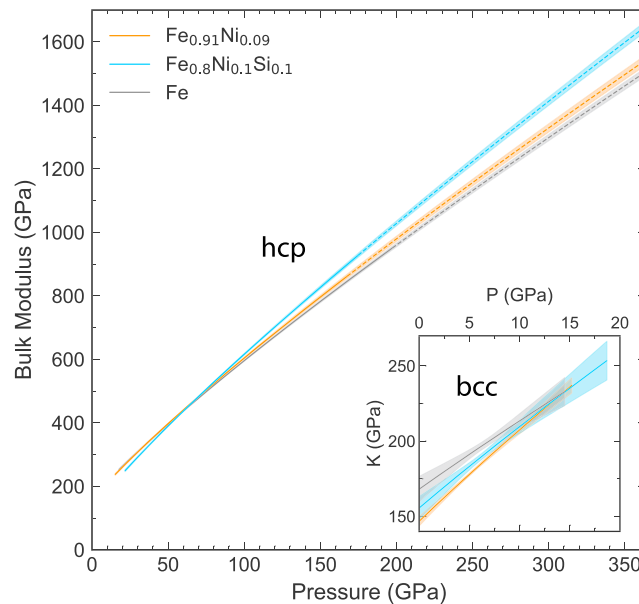
Figure 7. Isothermal bulk modulus at 300 K as a function of pressure for Vinet EOSs of hcp-Fe$_{0.91}$Ni$_{0.09}$, hcp-Fe$_{0.8}$Ni$_{0.1}$Si$_{0.1}$, and our refitting of hcp-Fe data reported in Dewaele et al. (2006). The uncertainties (shaded) reflect error propagation that includes parameter correlations. Inset: Isothermal bulk modulus at 300 K as a function of pressure for Vinet EOSs of bcc-Fe$_{0.91}$Ni$_{0.09}$, bcc-Fe$_{0.8}$Ni$_{0.1}$Si$_{0.1}$, and our fit of bcc-Fe data reported in Dewaele et al. (2006).

in Figures 6b–6e. The resulting EOS parameters and correlations from our fit to the hcp-Fe pressure-volume data from Dewaele et al. (2006) are given in Table 1 and supporting information Table S6, respectively. In Figure 6c, note the decrease in correlation between K_T and K'_T at 50 GPa, compared to that at 0 GPa (Figure 6b). At higher pressures, the confidence ellipses demonstrate positive correlation, and the correlation again increases with increasing pressure. At 50 GPa, the low correlation between K_T and K'_T allows the effect of alloying iron with Ni and Si to be more readily observed. Regardless of which pressure is chosen as an anchor
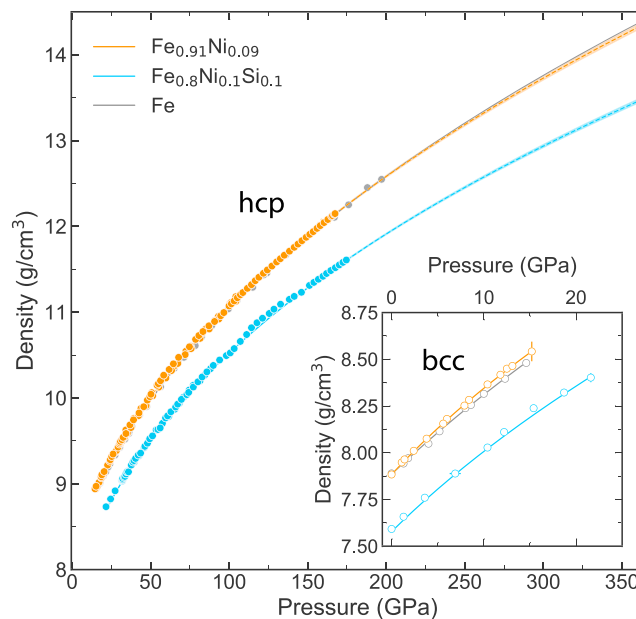
Figure 8. Density at 300 K as a function of pressure for bcc- and hcp-Fe$_{0.91}$Ni$_{0.09}$, bcc- and hcp-Fe$_{0.8}$Ni$_{0.1}$Si$_{0.1}$, and our refitting of hcp-Fe data reported in Dewaele et al. (2006), all assuming natural levels of ^{57}Fe enrichment. Open circles refer to bcc-structured data; filled circles refer to hcp-structured data. The uncertainties (shaded) reflect error propagation that includes parameter correlations.

Figure 9. A Birch plot of bulk sound speed v_ϕ as a function of density at 300 K. Isothermal Vinet EOSs for bcc- and hcp-$Fe_{0.91}Ni_{0.09}$, hcp-$Fe_{0.8}Ni_{0.1}Si_{0.1}$, and our refitting of hcp-Fe (Dewaele et al., 2006) are paired with thermal EOS parameters $\Theta_0 = 417$ K, $\gamma_0 = 2.0$, and $q = 1.0$ at 300 K. The uncertainties (shaded) reflect error propagation that includes parameter correlations for V_0, K_{T0}, and K'_{T0}. The hcp phases are plotted up to 364 GPa. Inset: Bulk sound spe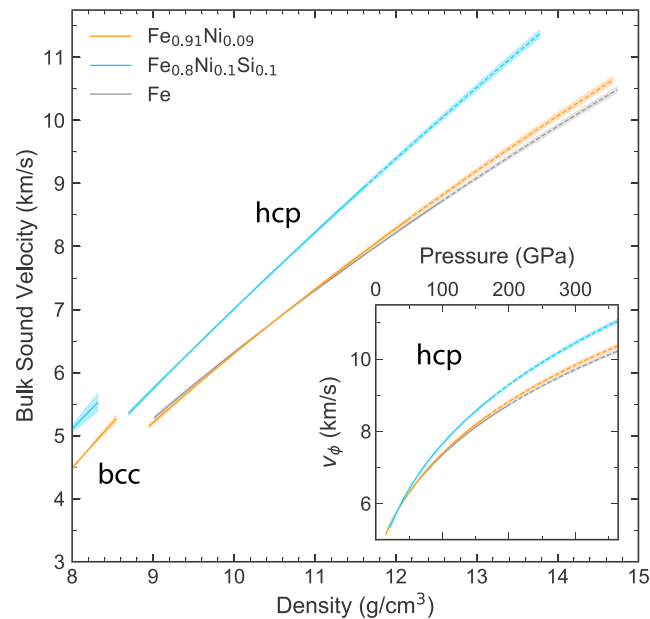ed at 300 K as a function of pressure for Vinet EOSs of hcp-$Fe_{0.91}Ni_{0.09}$, hcp-$Fe_{0.8}Ni_{0.1}Si_{0.1}$, and our refitting of hcp-Fe data reported in Dewaele et al. (2006).

for the EOS parameters, 9 at% nickel slightly increases the bulk modulus pressure derivative of hcp-iron, and 10 at% silicon noticeably increases the bulk modulus pressure derivative of hcp-$Fe_{0.91}Ni_{0.09}$. This effect is most evident in Figure 7 where the isothermal bulk moduli of bcc- and hcp-$Fe_{0.91}Ni_{0.09}$ (this study), $Fe_{0.8}Ni_{0.1}Si_{0.1}$ (this study), and Fe (Dewaele et al., 2006) are plotted as a function of pressure. The plotted uncertainties reflect error propagation that includes parameter correlations.

The density of bcc- and hcp-$Fe_{0.91}Ni_{0.09}$ (this study), $Fe_{0.8}Ni_{0.1}Si_{0.1}$ (this study), and Fe (Dewaele et al., 2006) are also plotted as a function of pressure with appropriate error propagation of the fit parameters (Figure 8). The densities of $Fe_{0.91}Ni_{0.09}$ and $Fe_{0.8}Ni_{0.1}Si_{0.1}$ are computed assuming natural iron isotopic abundance. We find that hcp-Fe and hcp-$Fe_{0.91}Ni_{0.09}$ are virtually indistinguishable in the pressure range investigated, but small measurable differences in their EOSs produce an hcp-$Fe_{0.91}Ni_{0.09}$ that is 0.3% lighter than pure iron at 330 GPa and 300 K. As expected, silicon substantially decreases the density of iron or of an iron-nickel alloy. The addition of 10 at% Si decreases the density of hcp-$Fe_{0.91}Ni_{0.09}$ by ~5% over all pressures investigated.

Bulk sound speed is of interest as it is related to the seismically observable compressional and shear sound velocities v_P and v_S. To determine bulk sound speed for hcp alloys, we first convert the experimentally constrained isothermal bulk modulus to an adiabatic bulk modulus with the thermal EOS parameters $\Theta_0 = 417$ K, $\gamma_0 = 2.0$, and $q = 1.0$. (See section 5.1 for these details.) For bcc alloys, we assume that the adiabatic and isothermal bulk moduli are approximately equal. We then calculate bulk sound speed at 300 K from the adiabatic bulk modulus combined with our experimentally determined density. We compare the bulk sound speeds of bcc- and hcp-$Fe_{0.91}Ni_{0.09}$ (this study), bcc- and hcp-$Fe_{0.8}Ni_{0.1}Si_{0.1}$ (this study), and hcp-Fe (Dewaele et al., 2006) as a function of density at 300 K using the natural isotopic abundance of iron in Figure 9. Compared to pure iron, the effect of alloying 9 at% nickel is negligible, whereas the addition of 10 at% silicon increases the bulk sound speed. Furthermore, the difference between the bulk sound speed of the silicon alloy compared to that of hcp-Fe increases with increasing pressure. In particular, the bulk sound speed of hcp-$Fe_{0.8}Ni_{0.1}Si_{0.1}$ increases from being 1.7% higher than hcp-Fe at 30 GPa to being 5.5% higher than hcp-Fe at 150 GPa.

Table 2
Density, Adiabatic Bulk Modulus, and Bulk Sound Velocity Uncertainties at High Temperature at the Inner Core Boundary (330 GPa)

	Fe			$Fe_{0.91}Ni_{0.09}$			$Fe_{0.8}Ni_{0.1}Si_{0.1}$		
	ρ	K_s	v_ϕ	ρ	K_s	v_ϕ	ρ	K_s	v_ϕ
	(g/cm^3)	(GPa)	(km/s)	(g/cm^3)	(GPa)	(km/s)	(g/cm^3)	(GPa)	(km/s)
Uncertainty from V_0, K_{T0}, $K'^{a}_{T0'}$	0.012	11	0.042	0.021	15	0.056	0.016	1	0.055
Uncertainty from γ_0, q^b	0.020	6.0	0.029	0.019	5.8	0.028	0.018	4.9	0.025
Total uncertainty without P_{el} and P^c_{anh}	0.032	17	0.071	0.040	21	0.085	0.033	20	0.080

[a]The V_0, K_{T0}, and K'_{T0} contribution to uncertainties of ρ, K_s, and v_ϕ for Fe were obtained by fitting an EOS to the Dewaele et al. (2006) data set with MINUTI and extrapolating to 330 GPa and 5500 K with fixed γ_0 and q. Similarly, the V_0, K_{T0}, and K'_{T0} contribution to uncertainties of ρ, K_s, and v_ϕ for $Fe_{0.91}Ni_{0.09}$ and $Fe_{0.8}Ni_{0.1}Si_{0.1}$ were obtained by fitting data from this study with MINUTI and extrapolating to 330 GPa and 5500 K with fixed γ_0 and q. [b]The uncertainty from γ_0 and q was estimated repeating the fits in (a) using the range of γ_0 and q reported in Murphy et al. (2011): γ_0 = 1.9 with q = 0.8 and γ_0 = 2.1 with q = 1.2. [c]The total uncertainties on density, adiabatic bulk modulus, and bulk sound speed at high temperature are the range of values spanned by the uncertainty calculations in (a) and (b). The uncertainty due to electronic and anharmonic contributions to thermal pressure is not accounted for here but is included in Figure 10.

5. Extrapolation to Inner Core Conditions

Geophysical observations paired with seismic models provide constraints for the density, adiabatic bulk modulus, and bulk sound speed of the inner core (e.g., Dziewonski & Anderson, 1981; Kennett et al., 1995). Knowledge of these properties at inner core conditions is an essential aspect of constraining the composition of the inner core. The phases hcp-Fe and hcp-$Fe_{0.91}Ni_{0.09}$ are thought to be stable at inner core conditions (Sakai et al., 2011; Tateno et al., 2010, 2012). $Fe_{0.8}Ni_{0.1}Si_{0.1}$ at inner core conditions is thought to adopt an hcp structure or a mixture of hcp and B2 phases (Fischer et al., 2013; Fischer & Campbell, 2015; Sakai et al., 2011; Tateno et al., 2015), where the B2 phase of Fe-Si and Fe-Ni-Si becomes more favorable as Si content or temperature is increased. We combine our 300 K equations of state with existing thermal parameters to obtain high-temperature equations of state from which we can estimate the density, adiabatic bulk modulus, and bulk sound speed of hcp-$Fe_{0.91}Ni_{0.09}$ and $Fe_{0.8}Ni_{0.1}Si_{0.1}$ at inner core conditions. We then place constraints on the composition of Earth's inner core by combining these results with available data on light-element alloys of iron and geophysical observations.

5.1. Thermal EOS

We extrapolate to inner core conditions with a thermal EOS,

$$P(V, T) = P_{300K}(V) + \Delta P_{Th}(V, T), \tag{1}$$

where $P_{300K}(V)$ is the 300 K Vinet EOS, and the thermal pressure $\Delta P_{Th}(V, T)$ is approximated using the following terms: a Debye model for vibrational energy, which is a quasi-harmonic model of the vibrations referred to as the Mie-Grüneisen-Debye EOS, as well as electronic (P_{el}) and anharmonic (P_{anh}) terms (Sturhahn, 2017),

$$\Delta P_{Th}(V, T) = P_{Th}(V, T) - P_{Th}(V, 300K) \tag{2}$$

and

$$P_{Th}(V, T) = \frac{\gamma(V)}{V}\left[9k_BT\left(\frac{T}{\Theta(V)}\right)^3 \int_0^{\Theta(V)/T} \frac{x^3 dx}{e^x - 1} + \frac{9}{8}k_B\Theta(V)\right] + P_{el} + P_{anh}. \tag{3}$$

We express the Grüneisen parameter $\gamma(V)$ with a volume dependent scaling law,

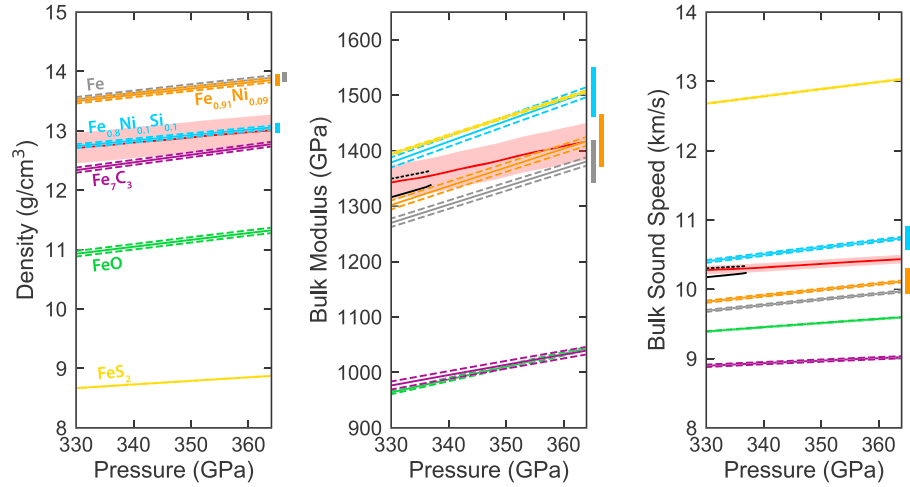$$\gamma(V) = \gamma_0 \left(\frac{V}{V_0}\right)^q, \tag{4}$$

Figure 10. Thermal EOSs for hcp-$Fe_{0.91}Ni_{0.09}$, $Fe_{0.8}Ni_{0.1}Si_{0.1}$ (this study), and Fe (Dewaele et al., 2006) are extrapolated to inner core conditions to calculate density ρ, adiabatic bulk modulus K_S, and bulk sound speed v_ϕ as a function of pressure at 5500 K (see text for details). Estimated electronic and anharmonic contributions to thermal pressure are included. Bars (right) represent uncertainty due to EOS parameters for hcp-Fe, $Fe_{0.91}Ni_{0.09}$, and $Fe_{0.8}Ni_{0.1}Si_{0.1}$. Upper and lower dashed lines represent -500 K and +500 K, respectively. We compare to the seismic model AK135-F (red line; Kennett et al., 1995) with estimated uncertainties for ρ (2%), K_S (2.3%), and v_ϕ (0.6%; Deuss, 2008; Masters & Gubbins, 2003). We include K_S and v_ϕ of the eastern (Bin 3, black dashed line) and western (Bin 6, black solid line) hemispheres of the inner core, as determined by combining v_P (Attanayake et al., 2014) with ρ and v_S from AK135-F. The ρ, K_S, and v_ϕ from thermal EOSs FeO (Fischer et al., 2011), Fe_7C_3 (Chen et al., 2012), and FeS_2 (Thompson et al., 2016) are included.

where γ_0 is the Grüneisen parameter at 1 bar and q is a scaling parameter. We express the Debye temperature as

$$\Theta(V) = \Theta_0 \exp\left[\frac{\gamma_0 - \gamma(V)}{q}\right]. \tag{5}$$

A nuclear resonant inelastic X-ray scattering (NRIXS) study to 171 GPa determined the phonon density of states of hcp-Fe as a function of volume, from which the ambient pressure Grüneisen parameter $\gamma_0 = 2.0 \pm 0.10$ and the scaling parameter $q = 1 \pm 0.2$ were determined (Murphy et al., 2011). We apply these values of γ_0 and q to the equations of state for hcp-$Fe_{0.91}Ni_{0.09}$, $Fe_{0.8}Ni_{0.1}Si_{0.1}$, and Fe. For hcp-$Fe_{0.91}Ni_{0.09}$ and $Fe_{0.8}Ni_{0.1}Si_{0.1}$, we assume the pure iron Debye temperature $\Theta_0 = 417$ K (Dewaele et al., 2006). The thermal equation of state parameters used for hcp-$Fe_{0.91}Ni_{0.09}$, $Fe_{0.8}Ni_{0.1}Si_{0.1}$, and Fe are shown in Table 3.

At temperatures relevant to the inner core, electronic (P_{el}) and anharmonic (P_{anh}) contributions to the thermal pressure become nonnegligible. To account for this contribution, we estimate P_{el} and P_{anh} using ab initio calculations. For hcp-Fe, we use the theoretically determined hcp-Fe P_{el} and P_{anh} from Dewaele et al. (2006). As calculations constraining the electronic and anharmonic contributions to thermal pressure for Fe-Ni alloys are limited, we estimate P_{el} and P_{anh} of hcp-$Fe_{0.91}Ni_{0.09}$ and $Fe_{0.8}Ni_{0.1}Si_{0.1}$ as those of hcp-Fe from Dewaele et al. (2006).

Density ρ at inner core conditions was calculated as a function of pressure and temperature from the hcp-Fe, $Fe_{0.91}Ni_{0.09}$, and $Fe_{0.8}Ni_{0.1}Si_{0.1}$ thermal equations of state. Natural isotopic enrichment was assumed for density calculations. Isothermal bulk modulus K_T was calculated from the thermal EOS,

$$K_T = -V\left(\frac{\partial P}{\partial V}\right)_T. \tag{6}$$

The adiabatic bulk modulus at inner core conditions, which can be compared with seismic models, was calculated with

$$K_S = K_T(1 + \gamma\alpha T), \tag{7}$$

where the thermal expansion α is calculated from the thermal EOS with

$$\alpha = \frac{1}{V}\left(\frac{\partial V}{\partial T}\right)_P, \tag{8}$$

Table 3
Thermal Equation of State Parameters Used to Extrapolate to Inner Core Conditions

Phase	V_0 (Å³)	K_0 (GPa)	K_0'	Θ_0 (K)	γ_0	q
hcp-Fe$_{0.91}$Ni$_{0.09}$[a,b]	22.505(42)	157.5(39)	5.61(10)	417[c]	2.0(1)[d]	1.0(2)[d]
hcp-Fe$_{0.8}$Ni$_{0.1}$Si$_{0.1}$[a,b]	22.952(72)	125.2(46)	6.38(12)	417[c]	2.0(1)[d]	1.0(2)[d]
hcp-Fe[a,c]	22.428(98)	163.4(79)	5.38(16)	417	2.0(1)[d]	1.0(2)[d]
B1-FeO[a,e]	20.352	149.4(10)	3.60(4)	417	1.41(5)	0.5
Fe$_7$C$_3$[a,f]	182.87(38)	307(6)	3.2(1)	920(140)	2.57(5)	2.2(5)
FeS$_2$[g]	158.59(7)	139.7(15)	5.69(19)	624(14)	1.39	2.04(28)

[a]The electronic and anharmonic contributions to thermal pressure are approximated by adding the theoretically determined P_{el} and P_{anh} of hcp-Fe (Dewaele et al., 2006) to the pressure. [b]This study: X-ray diffraction (XRD) at 300 K up to 167 GPa (hcp-Fe$_{0.91}$Ni$_{0.09}$) and 175 GPa (hcp-Fe$_{0.8}$Ni$_{0.1}$Si$_{0.1}$). [c]Dewaele et al. (2006): XRD at 300 K up to 205 GPa and ab initio calculations. [d]Murphy et al. (2011): XRD and NRIXS at 300 K up to 171 GPa. [e]Fischer et al. (2011): XRD with laser heating up to 156 GPa and 3100 K. [f]Chen et al. (2012): XRD at ambient temperature up to 167 GPa. [g]Thompson et al. (2016): XRD with laser heating up to 80 GPa and 2400 K. The electronic and anharmonic contribution to thermal pressure (A_2) as reported in Thompson et al. (2016) is included in this treatment.

and the Grüneisen parameter γ is calculated with equation (4). The bulk sound speed at inner core conditions, which is related to v_S and v_P, is then calculated by

$$v_\Phi = \left(\frac{K_S}{\rho}\right)^{1/2} = \left(v_P^2 - \frac{4}{3}v_S^2\right)^{1/2},$$

(9)

where the density ρ is calculated with natural isotopic abundance.

5.2. Iron Alloys at Inner Core Conditions

We use a few recent studies to estimate a plausible range of inner core temperatures. Although large discrepancies exist in reported inner core boundary (ICB) temperatures, one can use them as bounds in this analysis. For instance, Anzellini et al. (2013) report an ICB temperature of 6,230 ± 500 K for a pure iron core. Zhang et al. (2016) measured the melting temperature of compressed iron and hcp-Fe$_{0.9}$Ni$_{0.1}$ samples using synchrotron Mössbauer spectroscopy and a fast temperature readout spectrometer (Zhang et al., 2016). From these measurements, they estimate an upper bound for the ICB temperature of 5,500 ± 200 K. The studies by Zhang et al. (2016) were conducted on Fe$_{0.91}$Ni$_{0.09}$ samples from the same synthesis as those used in this study. It is also well known that the addition of light elements to hcp-iron can lower the melting temperature. For instance, silicon may depress the melting point of hcp-iron by 0–400 K, and sulfur may depress the melting point of hcp-iron by 900–1200 K (as reviewed in Fischer, 2016). As the change in temperature with radius in the inner core is thought to be small in comparison to the inner core temperature uncertainty (Brown & Shankland, 1981; Pozzo et al., 2014), we assume a uniform temperature in our analysis. For these reasons, we assess the compositional constraints using ICB temperatures of 5000, 5500, and 6000 K. The density, adiabatic bulk modulus, and bulk sound speed of hcp-Fe, Fe$_{0.91}$Ni$_{0.09}$, and Fe$_{0.8}$Ni$_{0.1}$Si$_{0.1}$, including their uncertainties, are thus calculated along the inner core pressure gradient from 330 to 364 GPa (Figure 10).

To calculate the uncertainty on density, adiabatic bulk modulus, and bulk sound speed from the hcp-Fe, Fe$_{0.91}$Ni$_{0.09}$, and Fe$_{0.8}$Ni$_{0.1}$Si$_{0.1}$ thermal equations of state, we propagate uncertainty from our isothermal EOS fit parameters V_0, K_{T0}, K_{T0}' and fix $\gamma_0 = 2.0$ with $q = 1.0$ (Murphy et al., 2011) using MINUTI. To estimate the uncertainty from γ_0 and q, we repeat this calculation using $\Theta_0 = 417$ K and the range of γ_0 and q reported in Murphy et al. (2011): $\gamma_0 = 1.9$ with $q = 0.8$ and $\gamma_0 = 2.1$ with $q = 1.2$ (Figure S4). The uncertainty contributions from V_0, K_{T0}, and K_{T0}' and from γ_0 and q are listed in Table 2. The uncertainty contributions due to the isothermal EOS parameters V_0, K_{T0}, and K_{T0}' for hcp-Fe, hcp-Fe$_{0.91}$Ni$_{0.09}$, and hcp-Fe$_{0.8}$Ni$_{0.1}$Si$_{0.1}$ are found to be of similar magnitude to the uncertainty due to γ_0 and q, which highlights the importance of accurately constraining the parameters V_0, K_{T0}, and K_{T0}' to obtain reliable thermal equations of state. One of the greatest sources of uncertainty is due to the electronic and anharmonic contributions to the thermal pressure, which are not well constrained (e.g., Alfè et al., 2001; Fei et al., 2016; Martorell, Vočadlo, et al., 2013; Martorell, Brodholt, et al., 2013; Martorell et al., 2016; Moustafa et al., 2017). To account for this, we enlarge our error bars on density,
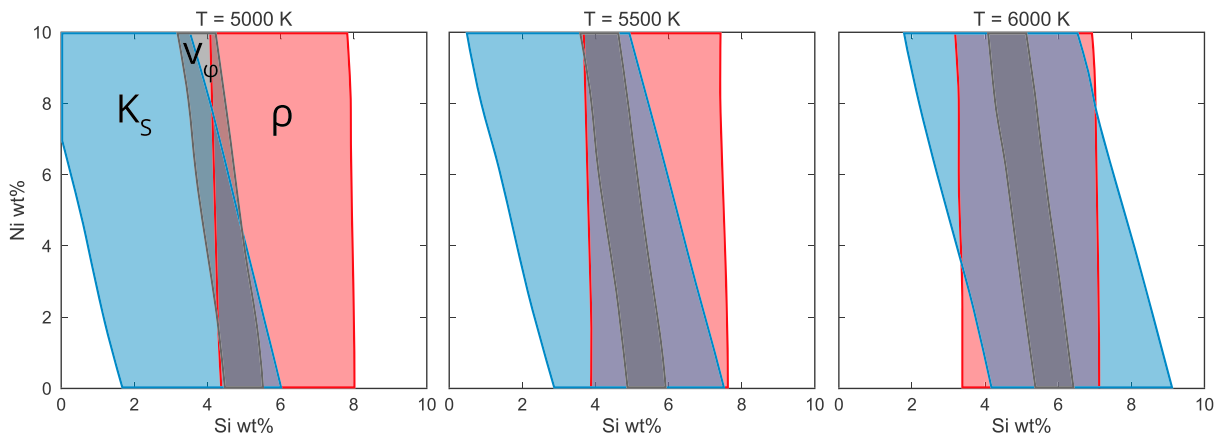
Figure 11. A range of inner core compositions in the Fe-Ni-Si system using experimental constraints on hcp-Fe, $Fe_{0.91}Ni_{0.09}$, and $Fe_{0.8}Ni_{0.1}Si_{0.1}$ with a linear mixing model. The regions represent agreement with the seismic model AK135-F within 2% of the density (red), 0.6% of the bulk sound speed (gray), and 2.3% of the adiabatic bulk modulus (blue). Seismically consistent compositions lie within the intersection of the three regions. Estimated electronic and anharmonic contributions to thermal pressure are included. Pressure is fixed at 330 GPa. See text for more details.

adiabatic bulk modulus, and bulk sound speed. The total uncertainty on density, adiabatic bulk modulus, and bulk sound speed for these three alloys at inner conditions is denoted by the vertical bars to the right of each panel in Figure 10.

To compare with the inner core, we plot density, adiabatic bulk modulus, and bulk sound speed from AK135-F as a function of pressure (Kennett et al., 1995) in red in Figure 10. The uncertainty of the inner core density is estimated at 2% by Masters and Gubbins (2003), and the uncertainty of the bulk sound speed of the inner core is estimated to be 0.6% by Deuss (2008). The uncertainty of the inner core adiabatic bulk modulus from AK135-F can then be estimated from error propagation to be 2.3%. The AK135-F model does not explicitly include pressure, so pressure is estimated from depth using the PREM model (Dziewonski & Anderson, 1981).

We first assess the constraints provided for Fe, $Fe_{0.91}Ni_{0.09}$, and $Fe_{0.8}Ni_{0.1}Si_{0.1}$. The density of hcp-$Fe_{0.8}Ni_{0.1}Si_{0.1}$ matches AK135-F throughout the inner core, suggesting $Fe_{0.8}Ni_{0.1}Si_{0.1}$ may be a reasonable composition for the Earth's inner core. While the adiabatic bulk modulus and bulk sound speed of hcp-$Fe_{0.8}Ni_{0.1}Si_{0.1}$ at the ICB are close to the uncertainty range of AK135-F, the pressure gradients of K_S and v_ϕ of $Fe_{0.8}Ni_{0.1}Si_{0.1}$ are significantly higher than those of AK135-F, a topic we will return to in the next section.

To examine the effect of other light elements, we include three thermal EOS studies in Figure 10: FeO (Fischer et al., 2011), Fe_7C_3 (Chen et al., 2012), and FeS_2 (Thompson et al., 2016). High-temperature DAC experiments by Fischer et al. (2011) investigated B1-structured FeO with X-ray diffraction and laser heating using a NaCl pressure medium and an iron pressure standard. Single-crystal DAC experiments at 300 K by Chen et al. (2012) investigated nonmagnetic hexagonal Fe_7C_3 with X-ray diffraction and synchrotron Mössbauer spectroscopy using a neon pressure medium and pressure marker. Chen et al. (2012) approximated the effects of temperature on nonmagnetic Fe_7C_3 using multianvil experiments on paramagnetic Fe_7C_3 by Nakajima et al. (2011). High-temperature DAC experiments by Thompson et al. (2016) investigated cubic FeS_2 (pyrite) with X-ray diffraction and laser heating using a KBr pressure medium and pressure calibrant. Thompson et al. (2016) constrained the cubic FeS_2 (pyrite) EOS at 300 K with a neon pressure medium and a gold pressure calibrant. The thermal equation of state parameters used for FeO, Fe_7C_3, and FeS_2 are shown in Table 3. While the methodology of our work allows for a systematic comparison of hcp-Fe, hcp-$Fe_{0.91}Ni_{0.09}$, and hcp-$Fe_{0.8}Ni_{0.1}Si_{0.1}$, the studies of FeO, Fe_7C_3, and FeS_2 were performed with varied methodology, so comparison to these alloys is more speculative.

The electronic and anharmonic contributions to thermal pressure for FeS_2 were constrained by Thompson et al. (2016) and are thus used for FeS_2. However, because these terms have not been constrained for FeO and Fe_7C_3, P_{el} and P_{anh} are approximated as the hcp-Fe P_{el} and P_{anh} terms reported by Dewaele et al. (2006). While hydrogen is suggested to be one of the light elements in Earth's core (e.g., Stevenson, 1977), Fe-Ni-H alloys were excluded here due to a sparsity of thermal EOSs with relevance to Earth's inner core conditions. The uncertainties on density, adiabatic bulk modulus, and bulk sound speed at high temperature for FeO, FeS_2, and Fe_7C_3 were not estimated as proper uncertainty propagation would require knowledge of the covariance matrix relating the fitted parameters V_0, K_{T0}, K'_{T0}, γ_0, and q.
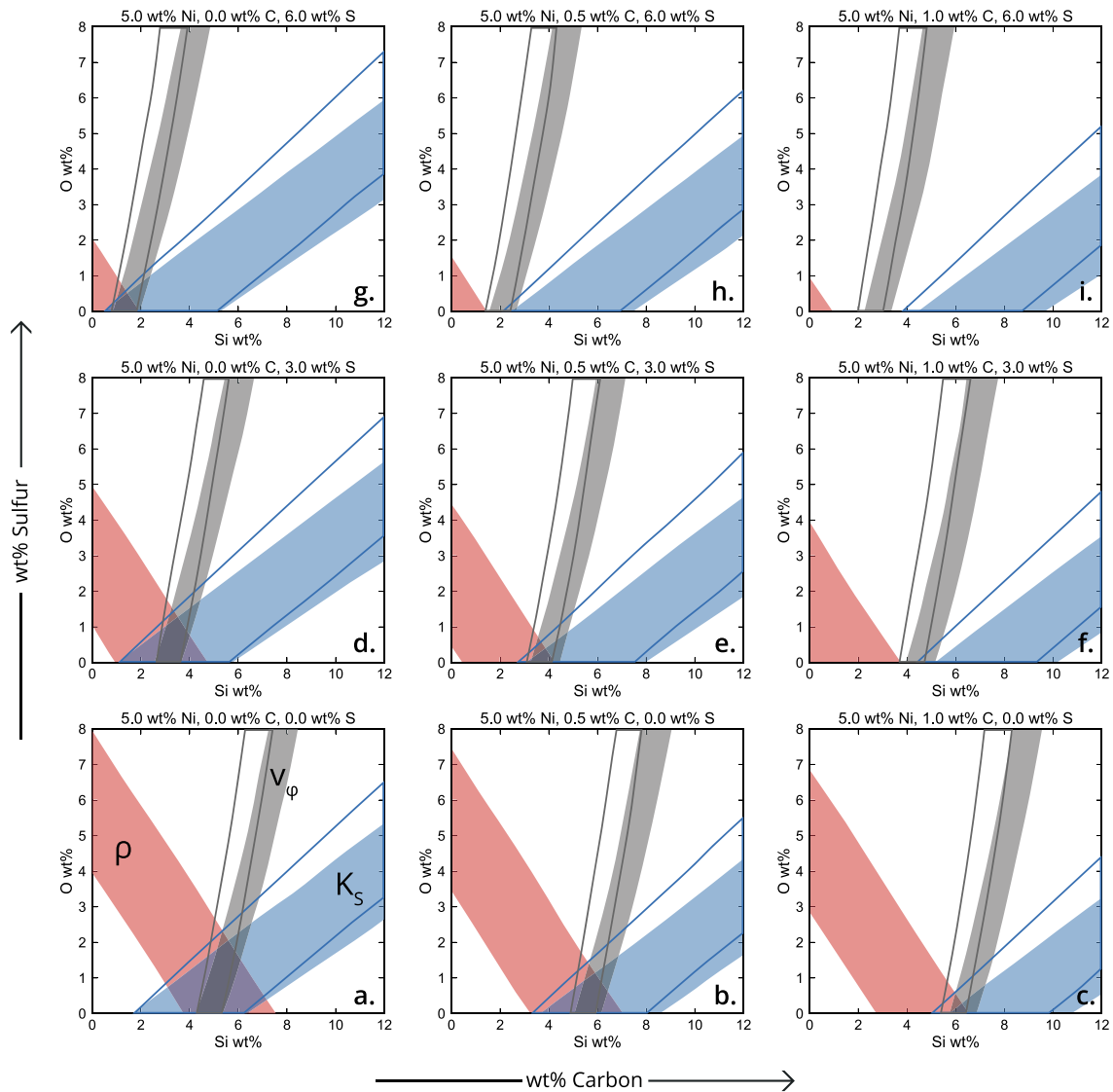
Figure 12. (a-i) A range of inner core compositions in the Fe-Ni-Si-O-C-S system using experimental constraints on hcp-Fe, hcp-Fe$_{0.91}$Ni$_{0.09}$, hcp-Fe$_{0.8}$Ni$_{0.1}$Si$_{0.1}$, Fe-O, Fe$_7$C$_3$, and FeS$_2$ with a linear mixing model (outlined regions) and a bulk aggregate model (shaded regions). The regions represent agreement with the seismic model AK135-F within 2% of the density (red), 0.6% of the bulk sound speed (gray), and 2.3% of the adiabatic bulk modulus (blue). Density is the same for both models. Seismically consistent compositions lie within the intersection of the density, adiabatic bulk modulus, and bulk sound speed regions in agreement with AK135-F. Estimated electronic and anharmonic contributions to thermal pressure are included. Nickel content is fixed at 5 wt%, and 5500 K and 330 GPa are assumed. See text for more details.

Concerning the stability of these phases in the inner core, Ozawa et al. (2011) find B2-FeO to be favored over B1-FeO above 240 GPa at 4000 K, thereby suggesting the B2 phase is stable in the inner core, and ab initio studies by Huang et al. (2018) propose *I4/mmm*-Fe$_2$O is energetically favorable above 270 GPa. However, experimental equations of state are not presently available for B2-FeO or *I4/mmm*-Fe$_2$O. Shock experiments by Ahrens and Jeanloz (1987) suggest that cubic pyrite is stable up to 320 GPa. While recent theory suggests that *C2/m*-FeS$_2$ may be stable at inner core conditions (Bazhanova et al., 2017), experimental equations of state are also not presently available for this phase. In a recent review, Li and Fei (2014) suggest that Fe$_7$C$_3$ is favored over Fe$_3$C as the liquidus phase of the Fe-C system at pressures above 7 GPa and therefore favored as a phase in the inner core.

The trends shown in Figure 10 suggest that neither oxygen nor carbon is likely to satisfy the geophysical constraints as the sole light element in the inner core. While it is not readily apparent from this figure whether sulfur alone could satisfy the density, adiabatic bulk modulus, and bulk sound speed of the inner core, it is clear

that none of the examined alloys match the seismic gradients of AK135-F. Next, we will explore and attempt to quantify geophysically permissible mixtures of these iron-rich light-element alloys.

5.3. Seismic and Experimental Constraints on Core Composition

5.3.1. Fe-Ni-Si System

We examine hypothetical compositions in the Fe-Ni-Si compositional space to determine whether silicon could be the dominant light element in the inner core. To do so, we apply a linear mixing model. Badro et al. (2007) propose linear mixing should hold for hcp-iron alloyed with low concentrations of light elements, and this approach has been applied to various solid iron alloys (e.g., Antonangeli et al., 2010, 2018; Badro et al., 2007; Fiquet et al., 2009; Ohtani, 2013). Linear mixing is therefore a reasonable approximation for a mixing of hcp-Fe, hcp-$Fe_{0.91}Ni_{0.09}$, and hcp-$Fe_{0.8}Ni_{0.1}Si_{0.1}$. Density can be calculated as

$$\rho_{avg} = \frac{\sum_i x_i m_i}{\sum_i \frac{x_i m_i}{\rho_i}}, \tag{10}$$

where x_i are atomic percents and m_i are the molecular weights. Voigt averaging is used to calculate the average adiabatic bulk modulus, and bulk sound speed is calculated from the adiabatic bulk modulus and density (equation (9)).

For each hypothetical composition, we compare the resulting density, adiabatic bulk modulus, and bulk sound speed to AK135-F at the ICB (330 GPa, Figure 10). If the density, adiabatic bulk modulus, and bulk sound speed of the given hypothetical composition fall strictly within 2% of AK135-F's density, 2.3% of adiabatic bulk modulus, and 0.6% of bulk sound speed at 330 GPa (Deuss, 2008; Masters & Gubbins, 2003), we consider the given hypothetical composition to be a possible core composition. Otherwise, the hypothetical composition is excluded. While all calculations are performed with atomic percent compositions, possible core compositions are selected and plotted as weight percent for literature comparison convenience.

We explore the compositional space within 0–10 wt% nickel and 0–12 wt% silicon. The resulting compositional space in agreement with AK135-F at the ICB at 5000, 5500, and 6000 K is plotted in Figure 11. If nickel content is fixed at 5 wt%, we find that a silicon content of 4.3–5.3 wt% satisfies the density, bulk modulus, and bulk sound speed of the ICB at 5500 K. With nickel content fixed at 5 wt%, a temperature of 5000 K lowers the allowable silicon content to 4.2–4.8 wt%, and a temperature of 6000 K raises the allowable silicon content to 4.7–5.8 wt%. While cosmochemical analyses suggest a Ni core content of 5 wt% (Allègre et al., 1995; McDonough, 2003), iron-nickel meteorites inferred to be remnants of differentiated protoplanets have variable nickel content. We find that any concentration of nickel in the investigated range of 0–10 wt% can satisfy the density, bulk modulus, and bulk sound speed at the ICB at 5500 and 6000 K. For a cooler ICB temperature of 5000 K, only up to 7.5 wt% nickel satisfies the density, bulk modulus, and bulk sound speed of the ICB. The nickel content has a small effect on the allowable silicon content in the inner core. Lowering the nickel content to 0 wt% would raise the allowable silicon content to 4.9–5.9 wt%, and raising the nickel content to 10 wt% would lower the allowable silicon content to 3.7–4.6 wt%. Therefore, we find an inverse relationship between the nickel and silicon content of the inner core.

5.3.2. Fe-Ni-Si-O-C-S System

As it is unlikely that the inner core contains only one light element, we extrapolate our analysis to the Fe-Ni-Si-O-C-S compositional space. While our Fe-Ni-Si compositional analysis is based on systematic experimental studies, this Fe-Ni-Si-O-C-S compositional analysis is necessarily based on studies with varied methodology and is therefore more speculative. While linear mixing may be a reasonable approximation for a mixing of hcp-Fe-Ni-Si with sufficiently small quantities of Ni and Si, immiscible phases and phases with different crystal structures are unlikely to follow a linear mixing model. A mixing of the phases hcp-Fe, B1-FeO, cubic FeS_2, and Fe_7C_3, which all have different crystal structures, may be better described by a bulk aggregate model. The accuracy of and deviation from these mixing models will be enlightened by future experimental studies on samples of intermediate compositions.

We therefore apply two basic models to explore the Fe-Ni-Si-O-C-S system: a linear mixing model and a bulk aggregate model. The calculation of density will be the same for both assumptions (see equation (10)). In the linear mixing case, Voigt averaging is used to calculate the average adiabatic bulk modulus as before.

Table 4
Iron Alloy Compositional Models in Agreement With the Density, Adiabatic Bulk Modulus, and Bulk Sound Velocity of AK135-F at the Inner Core Boundary

Corresponding panel in Figure 12	S (wt%, fixed)	C (wt%, fixed)	Bulk aggregate		Linear mixing	
			Si (wt%)	O (wt%)	Si (wt%)	O (wt%)
a	0	0	4.3−6.1	0.0−2.0	4.3−5.8	0.0−2.3
b	0	0.5	5.1−6.4	0.0−1.1	4.9−6.1	0.0−1.4
c	0	1	5.8−6.5	0.0−0.2	5.4−6.4	0.0−0.6
d	3	0	2.6−3.9	0.0−1.2	2.6−3.8	0.0−1.4
e	3	0.5	3.3−4.2	0.0−0.3	3.1−4.1	0.0−0.5
f	3	1	—	—	—	—
g	6	0	0.9−1.9	0.0−0.4	0.8−1.8	0.0−0.5
h	6	0.5	—	—	—	—
i	6	1	—	—	—	—

Note. Ni concentration is fixed at 5 wt%.

In the bulk aggregate case, Voigt-Reuss-Hill averaging is used to calculate the average adiabatic bulk modulus. As before, bulk sound speed is calculated from the adiabatic bulk modulus and density for both models (equation (9)).

For each hypothetical composition in the Fe-Ni-Si-O-C-S system, we compare the resulting density, adiabatic bulk modulus, and bulk sound speed to AK135-F at the ICB (330 GPa). We explore the compositional space within 0–10 wt% nickel, 0–12 wt% silicon, 0–8 wt% oxygen, 0–4 wt% carbon, and 0–12 wt% sulfur (Li & Fei, 2014; Sata et al., 2010). For subsequent results, we fix the nickel concentration of the bulk core composition at 5 wt% (Allègre et al., 1995; McDonough, 2003).

Select slices of the resulting compositional space in agreement with AK135-F at the ICB are plotted in Figure 12 and tabulated in Table 4. We find that as the carbon content of a hypothetical inner core composition increases, the allowable oxygen content decreases and silicon content increases. As the sulfur content of the inner core composition increases, the allowable oxygen and silicon contents decrease.

Using either a bulk aggregate or linear mixing assumption and a nickel content of 5 wt%, a silicon content of 4.3 to 5.3 wt% alone satisfies the density, bulk modulus, and bulk sound speed at the ICB, consistent with our analysis in just the Fe-Ni-Si compositional space (Figure 12, panel a). A maximum value of 1.0 wt% carbon is allowed with a bulk aggregate or linear mixing assumption, requiring the presence of up to 6.5 wt% silicon (Figure 12, panel c). A maximum value of 2.0 wt% oxygen is allowed with a bulk aggregate assumption (or 2.3 wt% with a linear mixing assumption). This oxygen content requires 5.6 wt% silicon (5.3 wt% with linear mixing) to also be present (Figure 12, panel a). We therefore find neither oxygen nor carbon can be the only light element in the inner core containing 5 wt% nickel. On the other hand, a maximum sulfur content of 7.5 wt% requires only 0.2 to 0.5 wt% silicon and no oxygen or carbon (with either a bulk aggregate or linear mixing assumption). Lower values of sulfur content (5 wt%) require a higher silicon content of 1.4 to 2.5 wt% silicon with a bulk aggregate assumption, or 1.5 to 2.6 wt% silicon with a linear mixing assumption (Figure 12, panel g).

We also explore the effect of varying nickel and temperature in the Fe-Ni-Si-O-C-S system. As the nickel content of the inner core increases, we find the allowable silicon content decreases and the allowable oxygen, carbon, and sulfur content increases (Figure S7 and Tables S8 and S9 in the supporting information). Temperature has a strong effect on the allowable core compositions. A cooler ICB temperature of 5000 K increases the seismic favorability of oxygen, carbon, and sulfur in the core, while a hotter temperature of 6000 K strongly decreases the seismic favorability of oxygen, carbon, and sulfur (Figures S8 and S9 and Tables S10 and S11 in the supporting information). Therefore, silicon is more seismically favorable as the dominant light element for hotter inner core boundary temperatures. This is consistent with data on the melting point depression due to the addition of light elements. Silicon is estimated to decrease the temperature at the inner core boundary by 0–400 K, oxygen by 700–1100 K, carbon by 600–800 K, and sulfur by 900–1200 K (as reviewed

in Fischer, 2016). Therefore, an inner core with predominately silicon as the light element would be associated with a hotter inner core boundary, and an inner core with predominately oxygen, carbon, or sulfur as the light element would be associated with a cooler inner core boundary.

5.3.3. Assessing the Effects of P_{el} and P_{anh}

We now assess the effects of P_{el} and P_{anh} on the density, adiabatic bulk modulus, and bulk sound speed of iron alloys at inner core conditions. We repeat the above calculations and analysis with thermal pressure approximated only as a Debye model of vibrational energy, that is, with the electronic and anharmonic contributions to the thermal pressure in equation (3) neglected. We refer to this model as the Vinet-Mie-Grüneisen-Debye (Vinet-MGD) EOS. We show the resulting density, adiabatic bulk modulus, and bulk sound speed at inner core conditions in Figure S5 in the supporting information. When P_{el} and P_{anh} are neglected, the properties change noticeably with respect to AK135-F. We find the absence of the P_{el} and P_{anh} contributions to the thermal pressure of hcp-$Fe_{0.8}Ni_{0.1}Si_{0.1}$ increase K_s and v_ϕ away from the values of AK135-F, which would, for all other things being equal, decrease the favorability of Si as a light element in the inner core. We also repeat the compositional mixing analysis with the Vinet-MGD EOS (i.e., neglecting P_{el} and P_{anh}). Several slices of the resulting allowable compositional space are shown in Figure S6 in the supporting information. Neglecting P_{el} and P_{anh} increases the overall compositional space in agreement with AK135-F. The overall effect of neglecting these terms is to decrease allowable concentration of Si while increasing the allowable concentrations of O, C, and S in the inner core. Therefore, accurately constraining the P_{el} and P_{anh} contributions to the thermal pressure of iron alloys is necessary to further constrain the composition of the inner core.

5.3.4. Seismic Gradients in the Inner Core

As previously mentioned, the gradients of adiabatic bulk modulus and bulk sound speed of all the examined iron alloys do not match those of AK135-F. If the average seismic gradients are true, we repeat the above mixing analysis at 364 GPa and 5500 K to assess permissible compositions. For this calculation, we include the electronic and anharmonic contributions to thermal pressure as previously detailed. Several slices of the resulting allowable compositional space are shown in Figure S10 in the supporting information. The overall effect of this analysis at 364 GPa is similar to the effect of neglecting P_{el} and P_{anh}. The allowable compositional space is generally increased, Si becomes less favorable, and O and C become more favorable. A recent study investigated the longitudinal variation of compressional wave speeds in the uppermost 80 km of the inner core (Attanayake et al., 2014). To draw comparisons with our analysis, we combine the compressional velocities from two of Attanayake et al.'s (2014) longitudinal bins (bin 3 in the eastern hemisphere and bin 6 in the western hemisphere) with the density and shear velocity of AK135-F to calculate the adiabatic bulk modulus and bulk sound speed. The longitudinal variation estimates are plotted as black dotted (east) and solid (west) lines in Figure 10. The K_S and v_ϕ gradients for all alloys appear to agree well with those reported for the upper inner core in the western hemisphere (bin 6) but not with those of the eastern hemisphere (bin 3; Attanayake et al., 2014). Thus, chemical and/or physical variations could exist laterally and radially, throughout the inner core. For example, there could be a gradient in composition or distinct phase/chemical boundaries within the inner core.

5.4. Discussion

We now compare our compositional mixing analysis at 5500 K at 330 GPa (Figure 12) to other proposed inner core compositions. Antonangeli et al. (2010) use inelastic X-ray scattering (IXS) results on the compressional wave velocity of $Fe_{0.89}Ni_{0.04}Si_{0.07}$ as a function of density (pressure) and suggest an inner core composition of 4–5 wt% Ni and 1–2 wt% Si, a composition also favored as a joint solution to geochemical, seismological, and mineral physics constraints of the outer core (Badro et al., 2015; Brodholt & Badro, 2017). We find that 1–2 wt% of Si alone is insufficient to match the density of the inner core. Later IXS and X-ray diffraction measurements up to 140 GPa determined the compressional waves of Fe alloyed with 9 wt% Si at 300 K (Antonangeli et al., 2018) and found that up to 3 ± 2 wt% Si could explain inner core properties for relatively high temperatures of 6200 to 6500 K. These silicon concentrations are lower than we suggest, as we find that an ICB temperature of 6000 K has an allowable silicon content of 4.7–5.8 wt%, and the concentration of silicon required increases with temperature. However, both our findings and those of Antonangeli et al. (2018) depend on how the electronic and anharmonic contributions to thermal pressure are modeled. Ab initio calculations by Martorell et al. (2016) find that the addition of silicon decreases density and increases both the compressional and shear velocities of iron at 360 GPa such that the density and velocities for a single Fe-Si composition cannot simultaneously satisfy seismic observations. They therefore suggest that silicon is unlikely to be the sole light element in the inner core, although this study did not consider the effects of nickel that we report here.

High-pressure partitioning experiments demonstrate that the simultaneous solubilities of Si and O increase substantially with temperature (Bouhifd & Jephcoat, 2011; Hirose et al., 2017; Siebert et al., 2012; Takafuji et al., 2004). To this end, a range of solutions containing both silicon and oxygen in our analysis would be permitted (Figure 12, panel a). Ab initio partitioning studies between solid and liquid iron containing Si, S, and O by Alfè et al. (2002, 2007) find weak partitioning of Si and S between liquid and solid iron and conclude that Si and S are insufficient to explain the density jump at the inner core boundary. Based on their finding that O is highly incompatible in solid iron and the seismically observed density jump reported by Masters and Gubbins (2003) of 6.5 $\pm$1.4 %, Alfè et al. (2007) estimate an inner core composition of 4.5 wt% of Si or S with trace amounts (0.06 wt%) of O and an outer core composition of 4.6 wt% of Si or S and 4.3 wt% of O. Our compositional analysis, which favors silicon and/or sulfur over oxygen and carbon in the inner core, is in agreement with this model (Figure 12, panels a, d, and g). An outer core containing larger amounts of silicon, such as 8–9 wt% (Fischer et al., 2015; Rubie et al., 2015), would not be favored by our compositional mixing analysis. A melting relation study by Komabayashi (2014) based on high-pressure and high-temperature experiments in the Fe-FeO system found that oxygen reduces the compressional wave velocity of liquid iron away from seismologically constrained values, thereby suggesting that the bulk outer core of the Earth is oxygen poor. This would suggest that the inner core is also oxygen poor. This is in agreement with the oxygen poor region of our compositional models (Figure 12, bottom of panels a–e and g).

The amount of carbon in the Earth is difficult to estimate as carbon may have accreted primarily as volatile hydrocarbons (Lodders, 2003) or as carbides or graphite which have greater thermal stabilities (Buchwald, 1975; Wood, 1993; Wood et al., 2013). Using a combination of cosmochemical, partitioning, density, and sound velocity studies, Wood et al. (2013) estimate the total upper carbon limit in the whole core at ~1 wt%. Ab initio partitioning calculations between iron and silicate melts by Zhang and Yin (2012) similarly estimate the carbon content in the whole core at 0.1–0.7 wt%. An ab initio study by Li et al. (2016) on the velocity and density of Fe_7C_3 found the density of Fe_7C_3 to be too low to be a major component of the inner core. Our compositional analysis is in qualitative agreement with Wood et al. (2013), Zhang and Yin (2012), and Li et al. (2016) as we find the maximum carbon content in the inner core to be 1.0 wt% coexisting with ~5 wt% Si. In contrast, Chen et al. (2014) suggest that the shear softening of Fe_7C_3 could explain the low shear velocity of the inner core. They propose a core composed of predominately Fe_7C_3, which would correspond to 8.4 wt% C in the inner core and a minimum of approximately 0.3 wt% of C in the bulk core. While our compositional analysis does not address shear velocities, the trends for density, bulk modulus, and bulk sound velocity do not favor an inner core carbon concentration of this magnitude.

6. Unit Cell Axial Ratio and Anisotropy

6.1. Overview

Seismic studies provide evidence for an anisotropic inner core (e.g., Attanayake et al., 2014; Deuss, 2014; Lythgoe et al., 2014). Various origins of this seismic anisotropy have been suggested, including preferred alignment of elastically anisotropic crystallites of iron alloys (e.g., Deuss, 2014; Hirose et al., 2013; Mainprice, 2015). However, the elastic anisotropy of hcp-Fe alloys are not very well constrained and currently debated. Elastic anisotropy of a material is directly determined by its single-crystal elastic modulus tensor (e.g., Grimvall, 1999), which can be experimentally or theoretically constrained by various approaches. One common measure of elastic anisotropy for hcp-structured materials is the ratio of compressional elastic moduli $\phi = C_{33}/C_{11}$, where the elastic moduli C_{11} and C_{33} are expressed in the condensed Voigt notation (e.g., Mainprice, 2015; Maupin & Park, 2015). However, hcp-iron is unstable at ambient pressure and temperature, and the high-pressure synthesis of an hcp-iron single crystal large enough to reliably determine elastic constants remains a challenge. Previous studies have attempted to experimentally constrain the relative magnitudes of C_{11} and C_{33} by inducing texture in polycrystalline hcp-iron in DACs and analyzing data collected at a range of angles compared to the direction of compression, using X-ray diffraction (Merkel et al., 2005; H. K. Mao et al., 1998; Singh et al., 1998) or IXS (Antonangeli, Occelli, et al., 2004; W. L. Mao et al., 2008). However, inducing texture in hcp-iron under such large compressions has been suggested to cause the material to behave plastically, so the results from such studies have been called into question (Antonangeli et al., 2006; Daymond et al., 1999; Li et al., 2004; Weidner et al., 2004; Wenk et al., 2000).

Multiple studies have suggested that the anisotropy of hcp-structured materials may be related to the ratio of the c to a unit cell parameters, which implies that the elastic anisotropy may be constrained by experimentally feasible c/a axial ratio measurements. For instance, Wenk et al. (1988) noted that at ambient pressure
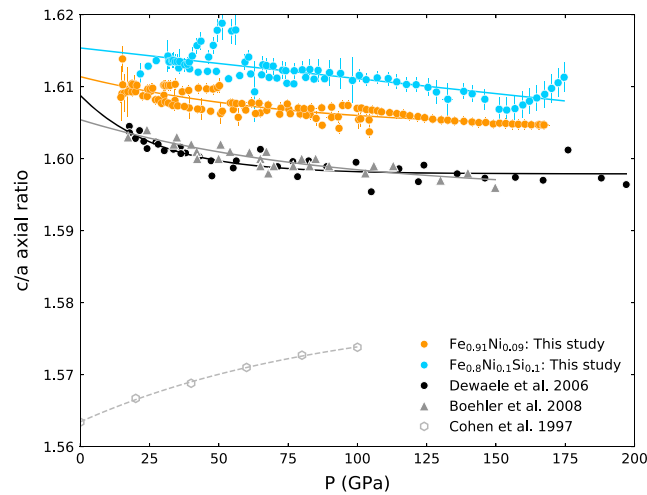
Figure 13. The c/a axial ratios of hcp-$Fe_{0.91}Ni_{0.09}$ (orange, this study) and $Fe_{0.8}Ni_{0.1}Si_{0.1}$ (blue, this study) determined with X-ray diffraction at 300 K fit with exponential functions (equation (11)). X-ray diffraction studies and exponential fits for pure hcp-Fe at 300 K by Dewaele et al., 2006 (2006; black) and Boehler et al., 2008 (2008; gray triangles) are included. The ab initio hcp-Fe study at 0 K by Cohen et al. (1997; gray open hexagons) is plotted to demonstrate the c/a change in slope and curvature as temperature rises from 0 to 300 K.

and temperature, the hcp-structured materials Zn and Cd which had c/a axial ratios greater than the ideal hcp value of 1.633 also had strong elastic anisotropy with $C_{33}/C_{11} \approx 0.4$. They also noted that the materials Ti and Zr which had c/a axial ratios less than 1.633 also had weak seismic anisotropy with $C_{33}/C_{11} \approx 1.15$. For reference, a $C_{33}/C_{11} = 1$ would correspond to a minimum compressional wave anisotropy. Steinle-Neumann et al. (2001) employ a conceptual argument, whereby the expansion of the c-axis with constant density may induce a softening along the c-axis, resulting in a decrease in C_{33}/C_{11}.

Theoretical calculations have noted a connection between c/a and anisotropy. Vočadlo et al. (2009) observe that in ab initio molecular dynamics calculations of elastic constants, it is critical to ensure that the simulated crystal structure is in equilibrium before a strain matrix is applied. They conclude that choice of the c/a axial ratio is therefore of particular importance to obtain realistic elastic constants in theoretical calculations. Grechnev et al. (2003) suggest theoretical calculations with high c/a yield calculations of high elastic anisotropy where $C_{33}/C_{11} < 1$. This argument is in agreement with that of Wenk et al. (1988), who also suggest that a high c/a is correlated with $C_{33}/C_{11} < 1$.

There is little consensus on the values and trends of axial ratios of iron alloys at ambient temperature (e.g., Asker et al., 2009; Fischer & Campbell, 2015; Gannarelli et al., 2005; Ono et al., 2010; Sha & Cohen, 2006), making the act of benchmarking the correlation between axial ratios and anisotropy difficult. We precisely determine the c/a axial ratio of hcp-$Fe_{0.91}Ni_{0.09}$ and hcp-$Fe_{0.8}Ni_{0.1}Si_{0.1}$ at 300 K as a function of pressure, compare to that of hcp-Fe, and examine the connection between the c/a axial ratio, its pressure derivative, and elastic anisotropy in hcp-structured materials.

6.2. Axial Ratios of Iron Alloys

The unit cell axial ratios (c/a) for hcp-$Fe_{0.91}Ni_{0.09}$ and hcp-$Fe_{0.8}Ni_{0.1}Si_{0.1}$ determined in this study from X-ray diffraction are shown in Figure 13 (see also Tables S1–S4 in the supporting information). We find that the hcp-$Fe_{0.91}Ni_{0.09}$ axial ratio ranges from 1.609 (20 GPa) to 1.604 (170 GPa) and the hcp-$Fe_{0.8}Ni_{0.1}Si_{0.1}$ ranges from 1.614 (30 GPa) to 1.608 (170 GPa). We compare to the axial ratios of pure hcp-Fe from Dewaele et al. (2006) and Boehler et al. (2008), which range from 1.604 (20 GPa) to 1.597 (170 GPa). The axial ratios of hcp-$Fe_{0.91}Ni_{0.09}$ and hcp-$Fe_{0.8}Ni_{0.1}Si_{0.1}$ decrease with pressure with a slope similar to that of hcp-Fe (Boehler et al., 2008; Dewaele et al., 2006), and all three materials have an axial ratio below the ideal hcp axial ratio of 1.633. The c/a axial ratios of the three materials are measurably distinct. The hcp-$Fe_{0.91}Ni_{0.09}$ axial ratio is offset from the pure iron axial ratio by +0.005 to +0.007, and the hcp-$Fe_{0.8}Ni_{0.1}Si_{0.1}$ axial ratio is further offset by roughly +0.005. Alloying iron with nickel therefore has a measurable effect on the c/a axial ratio of the alloy, as does alloying iron-nickel with silicon. This is in agreement with theoretical calculations from Asker et al. (2009) and Ekholm
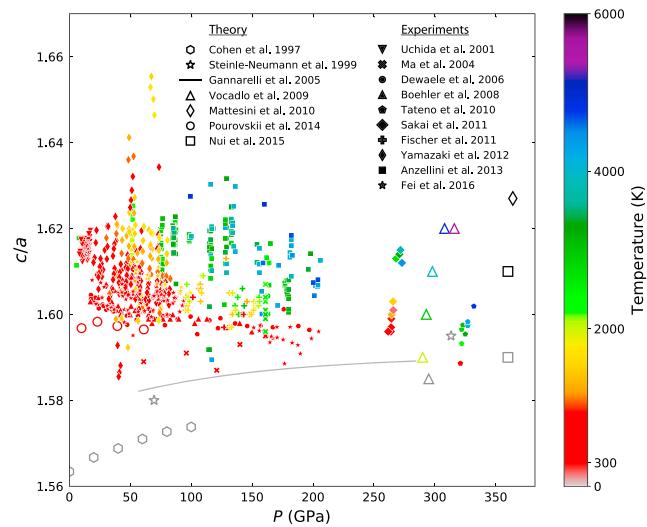
Figure 14. Axial ratios for hcp-Fe include diamond anvil studies (Anzellini et al., 2013; Boehler et al., 2008; Dewaele et al., 2006; Fei et al., 2016; Fischer et al., 2011; Ma et al., 2004; Sakai et al., 2011; Tateno et al., 2010), multianvil studies (Uchida et al., 2001; Yamazaki et al., 2012), and ab initio studies (Cohen et al., 1997; Gannarelli et al., 2005; Mattesini et al., 2010; Niu et al., 2015; Pourovskii et al., 2014; Steinle-Neumann et al., 1999; Vočadlo et al., 2009). Steinle-Neumann et al. (2001) is included in Figure S12.

et al. (2011) and existing experimental results from Lin et al. (2002), Tateno et al. (2012), Sakai et al. (2014), and Tateno et al. (2015).

Fischer and Campbell (2015) formulate a functional fit of the axial ratio data of hcp alloys in the Fe-Ni-Si system in volume, temperature, and compositional space based on a range of axial ratio measurements that include diamond anvil and multianvil cell experiments in various pressure media: He, Ne, KCl, NaCl, SiO_2, and MgO. We compare the Fischer and Campbell (2015) multicompositional c/a fit to our data as a function of volume in Figure S11 in the supporting information. The axial ratios of these three compositions decrease with increasing pressure (or decreasing volume), the addition of nickel to iron increases the axial ratio, and the further addition of silicon also increases the axial ratio. However, we find a more shallow decrease in axial ratio with compression than Fischer and Campbell (2015), which may be due to different pressure media. Many pressure media (e.g., NaCl) are less hydrostatic at 300 K. Helium, however, is much more hydrostatic at 300 K. Therefore, axial ratio measurements conducted in a helium pressure medium may more accurately constrain the axial ratio slope with pressure (or volume) at 300 K. The axial ratios of hcp-Fe (Boehler et al., 2008; Dewaele et al., 2006) and of hcp-$Fe_{0.91}Ni_{0.09}$ (this study) demonstrate a nonlinear curvature with pressure. We therefore fit the axial ratios of hcp-Fe, hcp-$Fe_{0.91}Ni_{0.09}$, and hcp-$Fe_{0.8}Ni_{0.1}Si_{0.1}$ with the empirical exponential decay function

$$\frac{c}{a}(P) = A + B \exp\left(\frac{-P}{C}\right). \tag{11}$$

Our fits are plotted with the hcp-iron alloy X-ray diffraction data in Figure 13.

In Figure 14, we compare the axial ratios of hcp-Fe reported from several studies at a range of temperatures. DAC X-ray diffraction experiments at 300 K were conducted by Dewaele et al. (2006) in a helium pressure medium and by Boehler et al. (2008) in various pressure media including Ar, Xe, KCl, and Al_2O_3 and annealed. Laser-heated DAC X-ray diffraction experiments were conducted by Ma et al. (2004) up to 161 GPa and 3000 K in NaCl, MgO, and Al_2O_3 pressure media; by Tateno et al. (2010) up to 377 GPa and 5700 K with no pressure medium; by Sakai et al. (2011) up to 273 GPa and 4490 K in a NaCl pressure medium; by Fischer et al. (2011) up to 156 GPa and 3100 K in a NaCl pressure medium; by Anzellini et al. (2013) up to 200 GPa and 4900 K in a KCl pressure medium; and by Fei et al. (2016) up to 205 GPa and 1800 K in Ne and MgO pressure media. Multianvil X-ray diffraction experiments by Uchida et al. (2001) up to 20 GPa and 1500 K and by Yamazaki et al. (2012) up to 80 GPa and 1900 K were conducted in MgO pressure media. We include ab initio hcp-Fe studies at 0 K from Cohen et al. (1997), Steinle-Neumann et al. (1999), and Gannarelli et al. (2005). Plotted ab initio hcp-Fe studies accounting for temperature effects include Steinle-Neumann et al. (2001), Vočadlo et al. (2009),
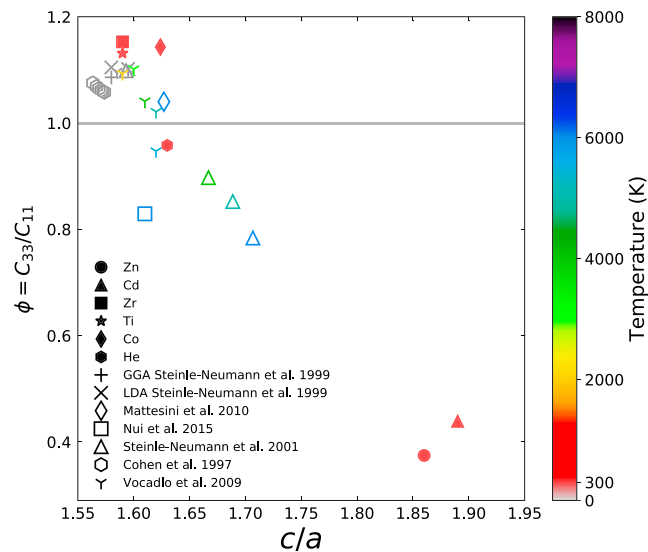
Figure 15. The c/a axial ratio and anisotropy measure ϕ for hcp-iron determined via ab initio calculations (Cohen et al., 1997; Mattesini et al., 2010; Niu et al., 2015; Steinle-Neumann et al., 1999; Vočadlo et al., 2009). We compare to hcp-structured materials Zn (Ledbetter, 1977), Cd, Zr, Ti (Wenk et al., 1988), Co, and He. (See supporting information for a description of Co and He c/a and ϕ values with associated references.) For a compressionally isotropic material, $\phi = 1$ (gray line). For an ideal hcp-structure, $c/a = 1.633$.

Mattesini et al. (2010), Niu et al. (2015), and Pourovskii et al. (2014). Steinle-Neumann et al. (2001) was excluded from Figure 14 for clarity but is shown in Figure S12 in the supporting information.

Several general conclusions can be drawn about the c/a axial ratios of pure iron. At 300 K, there is a weak decrease in the axial ratio of iron with pressure (e.g., Boehler et al., 2008; Dewaele et al., 2006; Fei et al., 2016; Steinle-Neumann et al., 2001). However, ab initio calculations at 0 K instead show a weak increase in the axial ratio of iron with pressure (Cohen et al., 1997; Gannarelli et al., 2005; Steinle-Neumann et al., 1999, 2001). Between 0 and 300 K, there appears to be a transition from a positive slope of c/a with pressure to a negative slope of c/a with pressure. As temperature increases, the slope of c/a with pressure appears to become increasingly negative (e.g., Fischer & Campbell, 2015). These studies suggest that both temperature and pressure influence the c/a axial ratio.

At constant temperature, we propose that the pressure-dependent functional form of c/a in equation (11) is generally applicable to hcp-Fe as an empirical fit. We fit the equation to the theoretically determined c/a axial ratio of hcp-Fe at 0 K from Cohen et al. (1997; Figure 13). Only the Cohen et al. (1997) ab initio data set contains a large enough number of data points at a constant temperature to obtain a reasonable fit. At 0 K, the sign of the scaling parameter B is negative. This is consistent with the observation that the slope of c/a with pressure transitions from positive at 0 K to negative at 300 K.

6.3. Relationship Between Axial Ratio and Anisotropy

To examine the connection between the c/a axial ratio and the anisotropy measure $\phi = C_{33}/C_{11}$, we plot ab initio studies of hcp-Fe which report both measures in Figure 15. We compare to the c/a axial ratio and anisotropy measure ϕ for other hcp-structured materials at 300 K and 0 GPa including Zn (Ledbetter, 1977), Cd, Zr, Ti (Wenk et al., 1988), Co (Antonangeli, Fiquet et al., 2004; Antonangeli, Benedetti, et al., 2008; Antonangeli, Krisch, et al., 2008; Crowhurst et al., 2006; Fujihisa & Takemura, 1996; Masumoto et al., 1966; McSkimin, 1955; Yu et al., 2012, see Figures S13-S15), and He (H. K. Mao et al., 1988; Loubeyre et al., 1993; Zha et al., 2004, see Figures S16-S18). While a correlation between the c/a axial ratio and the anisotropy measure $\phi = C_{33}/C_{11}$ has been suggested in several studies, several ab initio studies do not follow this trend. For instance, ab initio results are contradictory and often report different ϕ values for very similar c/a values, for example, Vočadlo et al. (2009) and Niu et al. (2015). Note that while Co and He have similar c/a axial ratios of ~1.63, they have noticeably different ϕ anisotropy values, with helium having $C_{33}/C_{11} \approx 0.95$ and cobalt having $C_{33}/C_{11} \approx 1.15$. We therefore conclude that while Figure 15 suggests a correlation between the c/a axial ratio and the anisotropy
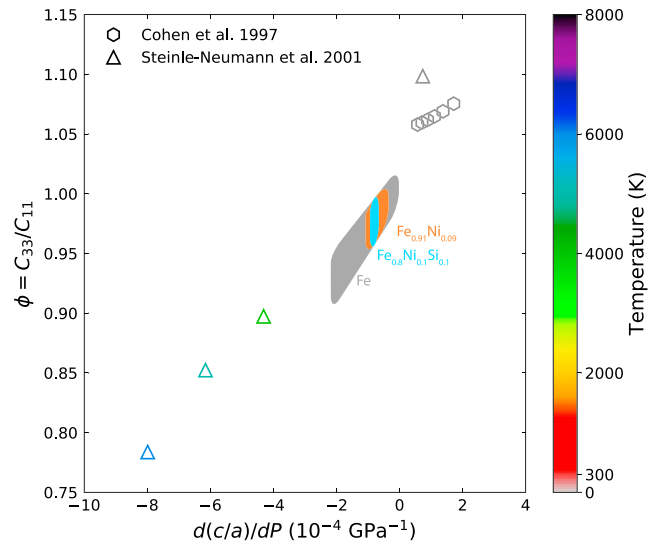
Figure 16. A positive correlation between the anisotropy measure ϕ and the pressure derivative of the axial ratio $d(c/a)/dP$ is suggested by the ab initio studies Cohen et al. (1997) at 0 K and Steinle-Neumann et al. (2001) at 0, 4000, 5000, and 6000 K. The shaded regions are a guide to the eye to indicate the $d(c/a)/dP$ of hcp-Fe, hcp-$Fe_{0.91}Ni_{0.09}$, and hcp-$Fe_{0.8}Ni_{0.1}Si_{0.1}$ at 300 K and their corresponding ϕ if they follow the same $d(c/a)/dP$ versus ϕ trend as the Cohen et al. (1997) or Steinle-Neumann et al. (2001) data. The hcp-Fe region is greater in size due to its larger c/a versus P curvature (see Figure 13), which results in a greater range of $d(c/a)/dP$ values. Regardless of the exact value of the slope of the correlation, a relationship between $d(c/a)/dP$ and ϕ will exist according to equation (12).

measure $\phi = C_{33}/C_{11}$, the relation between c/a and ϕ is likely nonunique, and c/a may be unable to reliably predict ϕ anisotropy.

We now examine the relationship between ϕ and the pressure derivative of c/a in Figure 16 for hcp-Fe. In the supporting information, the mathematical relationship between the elastic tensor components, C_{ij}, of hcp materials and the c/a axial ratio is shown to be

$$\frac{C_{11} - C_{33} + C_{12} - C_{13}}{(C_{11} + C_{12})C_{33} - 2C_{13}^2} = -\frac{d\ln(c/a)}{dP}. \tag{12}$$

The pressure derivative of c/a values at 0 K from Cohen et al. (1997) was calculated from the c/a versus pressure fit shown in Figure 13. As Steinle-Neumann et al. (2001) do not have enough reported c/a values for a given temperature to fit an exponential function, the pressure derivative of c/a was calculated from a linear fit of c/a versus pressure for 0, 4000, 5000, and 6000 K. The trends demonstrated in Figure 16 lend support for a positive correlation between $d(c/a)/dP$ and ϕ. If one uses the correlation in Figure 16 suggested by the cited ab initio studies, then the pressure derivatives of c/a for hcp-Fe (Dewaele et al., 2006), $Fe_{0.91}Ni_{0.09}$ (this study), and $Fe_{0.8}Ni_{0.1}Si_{0.1}$ (this study) at 300 K and up to 170 GPa as shown in Figure 13 would correspond to anisotropies of $\phi = 0.91 - 1.02$ as illustrated in Figure 16. Nevertheless, regardless of the exact value of the slope of the correlation, a relationship between $d(c/a)/dP$ and ϕ will exist according to equation (12).

7. Conclusions

We present a suite of powder X-ray diffraction data sets collected at 300 K on bcc- and hcp-$Fe_{0.91}Ni_{0.09}$ from 0 to 167 GPa and on bcc- and hcp-$Fe_{0.8}Ni_{0.1}Si_{0.1}$ from 0 to 175 GPa. Vinet equations of state were fit to the resulting pressure-volume data sets. By systematically comparing our findings to those of pure iron conducted under similar conditions (Dewaele et al., 2006), we constrain the effect of nickel and silicon on the density, bulk modulus, and bulk sound speed of iron alloys, which is a critical step in constraining the inner core's composition. By computing the confidence ellipses for the fitted EOS parameters at a range of pressures where hcp alloys are stable, we show that the addition of 9 at% Ni to hcp-Fe slightly increases the bulk modulus pressure derivative at all pressures. The further addition of 10 at% Si noticeably increases the pressure derivative of bulk modulus at all pressures.

The density, adiabatic bulk modulus, and bulk sound speed of hcp-$Fe_{0.91}Ni_{0.09}$ and hcp-$Fe_{0.8}Ni_{0.1}Si_{0.1}$ were extrapolated to 5500 K along the inner core pressure gradient from 330 to 364 GPa and compared to the seismic model AK135-F. We estimate the effect of the ICB temperature, as well as the electronic and anharmonic

contributions to thermal pressure, in our calculations. We applied a linear mixing model to the Fe-Ni-Si system to determine to what extent silicon is seismically consistent with the density, adiabatic bulk modulus, and bulk sound speed observations of the inner core at 330 GPa. We found that 4.3 to 5.3 wt% silicon alone could explain the density, adiabatic bulk modulus, and bulk sound speed of the inner core. Silicon concentrations above ∼6 wt% are not favored.

We extrapolated our compositional analysis to the Fe-Ni-Si-O-C-S system by applying both a bulk aggregate model and a linear mixing model at 330 GPa. A mixture of silicon and oxygen (with or without sulfur) could also explain the density, adiabatic bulk modulus, and bulk sound speed of the inner core. Our analysis points to a low oxygen content of the inner core (less than ∼2 wt%) as well as a low carbon content (less than 1 wt%). We find that an inner core with predominately silicon as the light element would be associated with a hotter ICB, and an inner core with predominately oxygen, carbon, or sulfur as the light element would be associated with a cooler ICB.

The inclusion of electronic and anharmonic contributions to thermal pressure has a noticeable effect on decreasing the allowable compositions. Therefore, constraining the electronic and anharmonic contributions to thermal pressure for a range of iron alloys at inner core conditions is necessary to further constrain core composition. Constraints on the shear properties and phase equilibria of iron alloys at inner core conditions, as well as constraints on the core temperature, are similarly important to further constrain core composition.

Finally, we find that hcp-$Fe_{0.91}Ni_{0.09}$ and hcp-$Fe_{0.8}Ni_{0.1}Si_{0.1}$ have greater c/a axial ratios compared to hcp-Fe at all measured pressures. We investigate the relationship between the c/a axial ratio and the compressional anisotropy measure $\phi = C_{33}/C_{11}$. Rather than relying on the c/a axial ratio to infer elastic anisotropy, which is shown to provide nonunique results, we propose a relationship between the pressure derivative of the c/a axial ratio and the anisotropy measure $\phi = C_{33}/C_{11}$. From our analysis, the pressure derivatives of c/a for hcp-Fe, $Fe_{0.91}Ni_{0.09}$, and $Fe_{0.8}Ni_{0.1}Si_{0.1}$ at 300 K and up to 170 GPa would correspond to anisotropies of $\phi = 0.91 - 1.02$. Future high-precision X-ray diffraction measurements of the pressure derivative of c/a at a range of pressures and temperatures will provide important constraints on the compressional anisotropy measure.

References

Ahrens, T. J., & Jeanloz, R. (1987). Pyrite: Shock compression, isentropic release, and composition of the Earth's core. *Journal of Geophysical Research*, *92*(B10), 10,363–10,375. https://doi.org/10.1029/JB092iB10p10363

Alfè, D., Gillan, M. J., & Price, G. D. (2002). Composition and temperature of the Earth's core constrained by combining ab initio calculations and seismic data. *Earth and Planetary Science Letters*, *195*(1-2), 91–98. https://doi.org/10.1016/S0012-821X(01)00568-4

Alfè, D., Gillan, M. J., & Price, G. D. (2007). Temperature and composition of the Earth's core. *Contemporary Physics*, *48*(2), 63–80. https://doi.org/10.1080/00107510701529653

Alfè, D., Price, G. D., & Gillan, M. J. (2001). Thermodynamics of hexagonal-close-packed iron under Earth's core conditions. *Physical Review B*, *64*, 045123. https://doi.org/10.1103/PhysRevB.64.045123

Allègre, C. J., Poirier, J. P., Humler, E., & Hofmann, A. W. (1995). The chemical composition of the Earth. *Earth and Planetary Science Letters*, *134*(3-4), 515–526. https://doi.org/10.1016/0012-821X(95)00123-T

Angel, R. J. (2000). Equations of state. *Reviews in Mineralogy and Geochemistry*, *41*(1), 35–59. https://doi.org/10.2138/rmg.2000.41.2

Antonangeli, D., Benedetti, L. R., Farber, D. L., Steinle-Neumann, G., Auzende, A. L., Badro, J., et al. (2008). Anomalous pressure evolution of the axial ratio c/a in hcp cobalt: Interplay between structure, magnetism, and lattice dynamics. *Applied Physics Letters*, *92*, 111911. https://doi.org/10.1063/1.2897038

Antonangeli, D., Krisch, M., Farber, D. L., Ruddle, D. G., & Fiquet, G. (2008). Elasticity of hexagonal-closed-packed cobalt at high pressure and temperature: A quasiharmonic case. *Physical Review Letters*, *100*, 085501. https://doi.org/10.1103/PhysRevLett.100.085501

Antonangeli, D., Krisch, M., Fiquet, G., Farber, D. L., Aracne, C. M., Badro, J., et al. (2004). Elasticity of cobalt at high pressure studied by inelastic x-ray scattering. *Physical Review Letters*, *93*, 215505. https://doi.org/10.1103/PhysRevLett.93.215505

Antonangeli, D., Merkel, S., & Farber, D. L. (2006). Elastic anisotropy in hcp metals at high pressure and the sound wave anisotropy of the Earth's inner core. *Geophysical Research Letters*, *33*, L24303. https://doi.org/10.1029/2006GL028237

Antonangeli, D., Morard, G., Paolasini, L., Garbarino, G., Murphy, C. A., Edmund, E., et al. (2018). Sound velocities and density measurements of solid hcp-Fe and hcp-Fe-Si (9 wt.%) alloy at high pressure: Constraints on the Si abundance in the Earth's inner core. *Earth and Planetary Science Letters*, *482*, 446–453. https://doi.org/10.1016/j.epsl.2017.11.043

Antonangeli, D., Occelli, F., Requardt, H., Badro, J., Fiquet, G., & Krisch, M. (2004). Elastic anisotropy in textured hcp-iron to 112 GPa from sound wave propagation measurements. *Earth and Planetary Science Letters*, *225*(1-2), 243–251. https://doi.org/10.1016/j.epsl.2004.06.004

Antonangeli, D., Siebert, J., Badro, J., Farber, D. L., Fiquet, G., Morard, G., & Ryerson, F. J. (2010). Composition of the Earth's inner core from high-pressure sound velocity measurements in Fe-Ni-Si alloys. *Earth and Planetary Science Letters*, *295*,(1-2) 292–296. https://doi.org/10.1016/j.epsl.2010.04.018

Anzellini, S., Dewaele, A., Mezouar, M., Loubeyre, P., & Morard, G. (2013). Melting of iron at Earth's inner core boundary based on fast X-ray diffraction. *Science*, *340*(6131), 464–466. https://doi.org/10.1126/science.1233514

Asanuma, H., Ohtani, E., Sakai, T., Terasaki, H., Kamada, S., Hirao, N., & Ohishi, Y. (2011). Static compression of $Fe_{0.83}Ni_{0.09}Si_{0.08}$ alloy to 374 GPa and $Fe_{0.93}Si_{0.07}$ alloy to 252 GPa: Implications for the Earth's inner core. *Earth and Planetary Science Letters*, *310*(1-2), 113–118. https://doi.org/10.1016/j.epsl.2011.06.034

Asker, C., Vitos, L., & Abrikosov, I. A. (2009). Elastic constants and anisotropy in FeNi alloys at high pressures from first-principles calculations. *Physical Review B*, *79*, 214112. https://doi.org/10.1103/PhysRevB.79.214112

Attanayake, J., Cormier, V. F., & De Silva, S. M. (2014). Uppermost inner core seismic structure—New insights from body waveform inversion. *Earth and Planetary Science Letters*, *385*, 49–58. https://doi.org/10.1016/j.epsl.2013.10.025

Badro, J., Brodholt, J. P., Piet, H., Siebert, J., & Ryerson, F. J. (2015). Core formation and core composition from coupled geochemical and geophysical constraints. *Proceedings of the National Academy of Sciences of the United States of America*, *112*(40), 12,310–12,314. https://doi.org/10.1073/pnas.1505672112

Badro, J., Fiquet, G., Guyot, F., Gregoryanz, E., Occelli, F., Antonangeli, D., & D'Astuto, M. (2007). Effect of light elements on the sound velocities in solid iron: Implications for the composition of Earth's core. *Earth and Planetary Science Letters*, *254*(1–2), 233–238. https://doi.org/10.1016/j.epsl.2006.11.025

Bazhanova, Z. G., Roizen, V. V., & Oganov, A. R. (2017). High-pressure behavior of the Fe-S system and composition of the Earth's inner core. *Physics-Uspekhi*, *60*(10), 1025–1032. https://doi.org/10.3367/UFNe.2017.03.038079

Boehler, R., Santamaría-Pérez, D., Errandonea, D., & Mezouar, M. (2008). Melting, density, and anisotropy of iron at core conditions: New x-ray measurements to 150 GPa. *Journal of Physics: Conference Series*, *121*(2), 022018. https://doi.org/10.1088/1742-6596/121/2/022018

Bouhifd, M. A., & Jephcoat, A. P. (2011). Convergence of Ni and Co metal-silicate partition coefficients in the deep magma-ocean and coupled silicon-oxygen solubility in iron melts at high pressures. *Earth and Planetary Science Letters*, *307*(3–4), 341–348. https://doi.org/10.1016/j.epsl.2011.05.006

Brodholt, J. P., & Badro, J. (2017). Composition of the low seismic velocity E' layer at the top of Earth's core. *Geophysical Research Letters*, *44*, 8303–8310. https://doi.org/10.1002/2017GL074261

Brown, J., & Shankland, T. (1981). Thermodynamic properties in the Earth as determined from seismic profiles. *Geophysical Journal of the Royal Astronomical Society*, *66*(3), 579–596. https://doi.org/10.1111/j.1365-246X.1981.tb04891.x

Buchwald, V. F. (1975). *Handbook of Iron Meteorites*, vol. 1. Berkeley, CA: University of California Press.

Campbell, A. J. (2016). Phase diagrams and thermodynamics of core materials. In H. Terasaki, & R. A. Fischer (Eds.), *Deep Earth: Physics and Chemistry of the Lower Mantle and Core* (vol. 15, pp. 191–199), Geophysical Monograph 217. Hoboken, NJ: John Wiley.

Chen, B., Gao, L., Lavina, B., Dera, P., Alp, E. E., Zhao, J., & Li, J. (2012). Magneto-elastic coupling in compressed Fe_7C_3 supports carbon in Earth's inner core. *Geophysical Research Letters*, *39*, L18301. https://doi.org/10.1029/2012GL052875

Chen, B., Li, Z., Zhang, D., Liu, J., Hu, M. Y., Zhao, J., et al. (2014). Hidden carbon in Earth's inner core revealed by shear softening in dense Fe_7C_3. *Proceedings of the National Academy of Sciences of the United States of America*, *111*(50), 17,755–17,758. https://doi.org/10.1073/pnas.1411154111

Cohen, R. E., Stixrude, L., & Wasserman, E. (1997). Tight-binding computations of elastic anisotropy of Fe, Xe, and Si under compression. *Physical Review B*, *56*(14), 8575–8589. https://doi.org/10.1103/PhysRevB.56.8575

Crowhurst, J. C., Antonangeli, D., Brown, J. M., Goncharov, A. F., Farber, D. L., & Aracne, C. M. (2006). Determination of the high pressure elasticity of cobalt from measured interfacial acoustic wave velocities. *Applied Physics Letters*, *89*(11), 111920. https://doi.org/10.1063/1.2220537

Daymond, M. R., Bourke, M. A. M., Dreele, R. B. V., Daymond, M. R., Bourke, M. A. M., & Dreele, R. B. V. (1999). Use of Rietveld refinement to fit a hexagonal crystal structure in the presence of elastic and plastic anisotropy. *Journal of Applied Physics*, *85*, 739–747. https://doi.org/10.1063/1.369154

Deuss, A. (2008). Normal mode constraints on shear and compressional wave velocity of the Earth's inner core. *Earth and Planetary Science Letters*, *268*(3-4), 364–375. https://doi.org/10.1016/j.epsl.2008.01.029

Deuss, A. (2014). Heterogeneity and anisotropy of Earth's inner core. *Annual Review of Earth and Planetary Sciences*, *42*, 103–126. https://doi.org/10.1146/annurev-earth-060313-054658

Dewaele, A., Loubeyre, P., & Mezouar, M. (2004). Equations of state of six metals above 94 GPa. *Physical Review B*, *70*, 094112. https://doi.org/10.1103/PhysRevB.70.094112

Dewaele, A., Loubeyre, P., Occelli, F., Mezouar, M., Dorogokupets, P., & Torrent, M. (2006). Quasihydrostatic equation of state of iron above 2 Mbar. *Physical Review Letters*, *97*, 215504. https://doi.org/10.1103/PhysRevLett.97.215504

Dorogokupets, P. I., & Oganov, a. R. (2006). Equations of state of Al, Au, Cu, Pt, Ta, and W and revised ruby pressure scale. *Doklady Earth Sciences*, *410*(1), 1091–1095. https://doi.org/10.1134/S1028334X06070208

Dziewonski, A. M., & Anderson, D. L. (1981). Preliminary reference Earth model. *Physics of the Earth and Planetary Interiors*, *25*(4), 297–356. https://doi.org/10.1016/0031-9201(81)90046-7

Ekholm, M., Mikhaylushkin, A. S., Simak, S. I., Johansson, B., & Abrikosov, I. A. (2011). Configurational thermodynamics of Fe–Ni alloys at Earth's core conditions. *Earth and Planetary Science Letters*, *308*(1–2), 90–96. https://doi.org/10.1016/j.epsl.2011.05.035

Fei, Y., Murphy, C., Shibazaki, Y., Shahar, A., & Huang, H. (2016). Thermal equation of state of hcp-iron: Constraint on the density deficit of Earth's solid inner core. *Geophysical Research Letters*, *43*, 6837–6843. https://doi.org/10.1002/2016GL069456

Fiquet, G., Badro, J., Gregoryanz, E., Fei, Y., & Occelli, F. (2009). Sound velocity in iron carbide (Fe3C) at high pressure: Implications for the carbon content of the Earth's inner core. *Physics of the Earth and Planetary Interiors*, *172*(1-2), 125–129. https://doi.org/10.1016/j.pepi.2008.05.016

Fischer, R. A. (2016). Melting of Fe alloys and the thermal structure of the core. In H. Terasaki & R. A. Fischer (Eds.), *Deep Earth: Physics and chemistry of the lower mantle and core* (vol. 1, pp. 3–12), Geophysical Monograph 217. Hoboken, NJ: John Wiley.

Fischer, R. A., & Campbell, A. J. (2015). The axial ratio of hcp Fe and Fe-Ni-Si alloys to the conditions of Earth's inner core. *American Mineralogist*, *100*(11-12), 2718–2724. https://doi.org/10.2138/am-2015-5191

Fischer, R. A., Campbell, A. J., Reaman, D. M., Miller, N. A., Heinz, D. L., Dera, P., & Prakapenka, V. B. (2013). Phase relations in the Fe-FeSi system at high pressures and temperatures. *Earth and Planetary Science Letters*, *373*, 54–64. https://doi.org/10.1016/j.epsl.2013.04.035

Fischer, R. A., Campbell, A. J., Shofner, G. A., Lord, O. T., Dera, P., & Prakapenka, V. B. (2011). Equation of state and phase diagram of FeO. *Earth and Planetary Science Letters*, *304*(3–4), 496–502. https://doi.org/10.1016/j.epsl.2011.02.025

Fischer, R. A., Nakajima, Y., Campbell, A. J., Frost, D. J., Harries, D., Langenhorst, F., et al. (2015). High pressure metal-silicate partitioning of Ni, Co, V, Cr, Si, and O. *Geochimica et Cosmochimica Acta*, *167*, 177–194. https://doi.org/10.1016/j.gca.2015.06.026

Fujihisa, H., & Takemura, K. (1996). Equation of state of cobalt up to 79 GPa. *Physical Review B*, *54*(1), 5–7. https://doi.org/10.1103/PhysRevB.54.5

Gannarelli, C. M. S., Alfè, D., & Gillan, M. J. (2005). The axial ratio of hcp iron at the conditions of the Earth's inner core. *Physics of the Earth and Planetary Interiors*, *152*(1-2), 67–77. https://doi.org/10.1016/j.pepi.2005.06.003

Grechnev, G. E., Ahuja, R., & Eriksson, O. (2003). Magnetic susceptibility of hcp iron and the seismic anisotropy of Earth's inner core. *Physical Review B*, *68*, 64414. https://doi.org/10.1103/PhysRevB.68.064414

Grimvall, G. (1999). *Thermophysical properties of materials*. Amsterdam: Elsevier.

Hirose, K., Labrosse, S., & Hernlund, J. (2013). Composition and state of the core. *Annual Review of Earth and Planetary Sciences*, *41*, 657–691. https://doi.org/10.1146/annurev-earth-050212-124007

Hirose, K., Morard, G., Sinmyo, R., Umemoto, K., Hernlund, J., Helffrich, G., & Labrosse, S. (2017). Crystallization of silicon dioxide and compositional evolution of the Earth's core. *Nature Publishing Group*, *543*, 99–102. https://doi.org/10.1038/nature21367

Holmes, N. C., Moriarty, J. A., Gathers, G. R., & Nellis, W. J. (1989). The equation of state of platinum to 660 GPa (6.6 Mbar). *Journal of Applied Physics*, *66*(7), 2962–2967. https://doi.org/10.1063/1.344177

Huang, S., Wu, X., & Qin, S. (2018). Stability and anisotropy of $(Fe_xNi_{1-x})_2O$ under high pressure and implications in Earth's and super-Earths' core. *Scientific Reports*, *8*, 236. https://doi.org/10.1038/s41598-017-18678-z

Kennett, B. L. N., Engdah, E. R., & Buland, R. (1995). Constraints on seismic velocities in the Earth from traveltimes. *Geophysical Journal International*, *122*, 108–124. https://doi.org/10.1111/j.1365-246X.1995.tb03540.x

Klotz, S., Chervin, J.-C., Munsch, P., & Le Marchand, G. (2009). Hydrostatic limits of 11 pressure transmitting media. *Journal of Physics D: Applied Physics*, *42*(7), 075413. https://doi.org/10.1088/0022-3727/42/7/075413

Komabayashi, T. (2014). Thermodynamics of melting relations in the system Fe-FeO at high pressure: Implications for oxygen in the Earth's core. *Journal of Geophysical Research: Solid Earth*, *119*, 4164–4177. https://doi.org/10.1002/2014JB010980

Ledbetter, H. M. (1977). Elastic properties of zinc: A compilation and a review. *Journal of Physical and Chemical Reference Data*, *6*, 1181–1203. https://doi.org/10.1063/1.555564

Li, J., & Fei, Y. (2014). Experimental constraints on core composition. In G. Schubert (Ed.), *Treatise on Geochemistry: Second Edition* (Vol. 3, pp. 527–557). Oxford, UK: Elsevier Inc. https://doi.org/10.1016/B978-0-08-095975-7.00214-X

Li, Y., Vočadlo, L., Brodholt, J., & Wood, I. G. (2016). Thermoelasticity of Fe_7C_3 under inner core conditions. *Journal of Geophysical Research: Solid Earth*, *121*, 5828–5837. https://doi.org/10.1002/2016JB013155

Li, L., Weidner, D. J., Chen, J., Vaughan, M. T., Davis, M., & Durham, M. D. B. (2004). X-ray strain analysis at high pressure: Effect of plastic deformation in MgO. *Journal of Applied Physics*, *95*, 8357–8365. https://doi.org/10.1063/1.1738532

Lin, J.-F. (2003). Static compression of iron-silicon alloys: Implications for silicon in the Earth's core. *Journal of Geophysical Research*, *108*(B1), 2045. https://doi.org/10.1029/2002JB001978

Lin, J.-f., Heinz, D. L., Campbell, A. J., Devine, J. M., Mao, W. L., & Shen, G. (2002). Iron-Nickel alloy in the Earth's core. *Geophysical Research Letters*, *29*(10), 1471. https://doi.org/10.1029/2002GL015089

Lodders, K. (2003). Solar system abundances and condensation temperatures of the elements. *The Astrophysical Journal*, *591*(2), 1220–1247. https://doi.org/10.1086/375492

Loubeyre, P., Letoullec, R., Pinceaux, J. P., Mao, H. K., Hu, J., & Hemley, R. J. (1993). Equation of state and phase diagram of solid [4]He from single-crystal X-ray diffraction over a large *P*- domain. *Physical Review Letters*, *71*(14), 2272–2275. https://doi.org/10.1103/PhysRevLett.71.2272

Lythgoe, K. H., Deuss, A., Rudge, J. F., & Neufeld, J. A. (2014). Earth's inner core: Innermost inner core or hemispherical variations? *Earth and Planetary Science Letters*, *385*, 181–189. https://doi.org/10.1016/j.epsl.2013.10.049

Ma, Y., Somayazulu, M., Shen, G., Mao, H.-K., Shu, J., & Hemley, R. J. (2004). In situ X-ray diffraction studies of iron to Earth-core conditions. *Physics of the Earth and Planetary Interiors*, *143-144*, 455–467. https://doi.org/10.1016/j.pepi.2003.06.005

Mainprice, D. (2015). Seismic anisotropy of the deep Earth from a mineral and rock physics perspective. In G. Schubert (Ed.), *Treatise on Geophysics: Second Edition* (Vol. 2, pp. 437–491). Oxford, UK: Elsevier B.V. https://doi.org/10.1016/B978-044452748-6.00045-6

Mao, H. K., Hemley, R. J., Wu, Y., Jephcoat, A. P., Finger, L. W., Zha, C. S., & Bassett, W. A. (1988). High-pressure phase diagram and equation of state of solid helium from single-crystal x-ray diffraction to 23.3 GPa. *Physical Review Letters*, *60*(25), 2649–2652. https://doi.org/10.1103/PhysRevLett.60.2649

Mao, H. K., Shu, J., Shen, G., Hemley, R. J., Li, B., & Singh, A. K. (1998). Elasticity and rheology of iron above 220 GPa and the nature of the Earth's inner core. *Nature*, *396*, 741–743. https://doi.org/10.1038/25506

Mao, W. L., Struzhkin, V. V., Baron, A. Q. R., Tsutsui, S., Tommaseo, C. E., Wenk, H.-R., et al. (2008). Experimental determination of the elasticity of iron at high pressure. *Journal of Geophysical Research*, *113*, B09213. https://doi.org/10.1029/2007JB005229

Mao, H. K., Wu, Y., Chen, L. C., Shu, J. F. & Jephcoat, A. P. (1990). Static compression of iron to 300 GPa and $Fe_{0.8}Ni_{0.2}$ alloy to 260 GPa: Implications for composition of the core. *Journal of Geophysical Research*, *95*(B13), 21,737–21,742. https://doi.org/10.1029/JB095iB13p21737

Martorell, B., Brodholt, J., Wood, I. G., & Vočadlo, L. (2013). The effect of nickel on the properties of iron at the conditions of Earth's inner core: Ab initio calculations of seismic wave velocities of Fe-Ni alloys. *Earth and Planetary Science Letters*, *365*, 143–151. https://doi.org/10.1016/j.epsl.2013.01.007

Martorell, B., Vočadlo, L., Brodholt, J., & Wood, I. G. (2013). Strong premelting effect in the elastic properties of hcp-Fe under inner-core conditions. *Science*, *342*, 466–468. https://doi.org/10.1126/science.1243651

Martorell, B., Wood, I. G., Brodholt, J., & Vočadlo, L. (2016). The elastic properties of hcp-$Fe_{1-x}Si_x$ at Earth's inner-core conditions. *Earth and Planetary Science Letters*, *451*, 89–96. https://doi.org/10.1016/j.epsl.2016.07.018

Masters, G., & Gubbins, D. (2003). On the resolution of density within the Earth. *Physics of the Earth and Planetary Interiors*, *140*(1–3), 159–167. https://doi.org/10.1016/j.pepi.2003.07.008

Masumoto, H., Saitô, H., & Kikuchi, M. (1966). Thermal expansion and temperature dependence of Young's modulus of single crystal of hexagonal cobalt (*Rep. 1319*). Tohoku Japan: Research Institute for Iron, Steel and Other Metals.

Mattesini, M., Belonoshko, A. B., Buforn, E., Ramírez, M., Simak, S. I., Udías, A., Mao, H. K., & Ahuja, R. (2010). Hemispherical anisotropic patterns of the Earth's inner core. *Proceedings of the National Academy of Sciences of the United States of America*, *107*(21), 9507–9512. https://doi.org/10.1073/pnas.1004856107

Maupin, V., & Park, J. (2015). Theory and observations—Seismic anisotropy. In G. Schubert (Ed.), *Treatise on Geophysics* (vol. 1, pp. 277–305). Oxford, UK: Elsevier B.V. https://doi.org/10.1016/B978-0-444-53802-4.00007-5

McDonough, W. F. (2003). Compositional model for the Earth's core. In R. W. Carlson (Ed.), *Treatise on Geochemistry* (Vol. 2, pp. 547–568). Oxford, UK: Elsevier Ltd. https://doi.org/10.1016/B0-08-043751-6/02015-6

McSkimin, H. J. (1955). Measurement of the elastic constants of single crystal cobalt. *Journal of Applied Physics*, *26*, 406–409. https://doi.org/10.1063/1.1722007

Merkel, S., Shu, J., Gillet, P., Mao, H.-k., & Hemley, R. J. (2005). X-ray diffraction study of the single-crystal elastic moduli of ϵ-Fe up to 30 GPa. *Journal of Geophysical Research*, *110*, B05201. https://doi.org/10.1029/2004JB003197

Moustafa, S. G., Schultz, A. J., Zurek, E., & Kofke, D. A. (2017). Accurate and precise ab initio anharmonic free-energy calculations for metallic crystals: Application to hcp Fe at high temperature and pressure. *Physical Review B*, *96*, 014117. https://doi.org/10.1103/PhysRevB.96.014117

Murphy, C. A., Jackson, J. M., Sturhahn, W., & Chen, B. (2011). Grüneisen parameter of hcp-Fe to 171 GPa. *Geophysical Research Letters*, *38*, L24306. https://doi.org/10.1029/2011GL049531

Nakajima, Y., Takahashi, E., Sata, N., Nishihara, Y., Hirose, K., Funakoshi, K. I., & Ohishi, Y. (2011). Thermoelastic property and high-pressure stability of Fe7C3: Implication for iron-carbide in the Earth's core. *American Mineralogist*, *96*(7), 1158–1165. https://doi.org/10.2138/am.2011.3703

Niu, Z.-W., Zeng, Z.-Y., Cai, L.-C., & Chen, X.-R. (2015). Study of the thermodynamic stability of iron at inner core from first-principles theory combined with lattice dynamics. *Physics of the Earth and Planetary Interiors*, *248*, 12–19. https://doi.org/10.1016/j.pepi.2015.09.002

Ohtani, E. (2013). Chemical and physical properties and thermal state of the core. In S.-I. Karato (Ed.), *Physics and chemistry of the deep Earth* (vol. 8, pp. 244–270). Chichester, UK: John Wiley.

Ono, S., Kikegawa, T., Hirao, N., & Mibe, K. (2010). High-pressure magnetic transition in hcp-Fe. *American Mineralogist*, *95*(5–6), 880–883. https://doi.org/10.2138/am.2010.3430

Ozawa, H., Takahashi, F., Hirose, K., Ohishi, Y., & Hirao, N. (2011). Phase transition of FeO and stratification in Earth's outer core. *Science*, *334*(6057), 792–794. https://doi.org/10.1126/science.1208265

Poirier, J.-P. (1994). Light elements in the Earth's outer core: A critical review. *Physics of the Earth and Planetary Interiors*, *85*(3–4), 319–337. https://doi.org/10.1016/0031-9201(94)90120-1

Pourovskii, L. V., Mravlje, J., Ferrero, M., Parcollet, O., & Abrikosov, I. A. (2014). Impact of electronic correlations on the equation of state and transport in ϵ-Fe. *Physical Review B - Condensed Matter and Materials Physics*, *90*(15), 155120. https://doi.org/10.1103/PhysRevB.90.155120

Pozzo, M., Davies, C., Gubbins, D., & Alfé, D. (2014). Thermal and electrical conductivity of solid iron and iron-silicon mixtures at Earth's core conditions. *Earth and Planetary Science Letters*, *393*, 159–164. https://doi.org/10.1016/j.epsl.2014.02.047

Prescher, C., & Prakapenka, V. B. (2015). DIOPTAS: A program for reduction of two-dimensional X-ray diffraction data and data exploration. *High Pressure Research*, *35*(3), 223–230. https://doi.org/10.1080/08957959.2015.1059835

Rubie, D. C., Jacobson, S. A., Morbidelli, A., Brien, D. P. O., Young, E. D., Vries, J. D., et al. (2015). Accretion and differentiation of the terrestrial planets with implications for the compositions of early-formed Solar System bodies and accretion of water. *Icarus*, *248*, 89–108. https://doi.org/10.1016/j.icarus.2014.10.015

Sakai, T., Ohtani, E., Hirao, N., & Ohishi, Y. (2011). Stability field of the hcp-structure for Fe, Fe-Ni, and Fe-Ni-Si alloys up to 3 Mbar. *Geophysical Research Letters*, *38*, L09302. https://doi.org/10.1029/2011GL047178

Sakai, T., Takahashi, S., Nishitani, N., Mashino, I., Ohtani, E., & Hirao, N. (2014). Equation of state of pure iron and $Fe_{0.9}Ni_{0.1}$ alloy up to 3 Mbar. *Physics of the Earth and Planetary Interiors*, *228*, 114–126. https://doi.org/10.1016/j.pepi.2013.12.010

Sata, N., Hirose, K., Shen, G., Nakajima, Y., Ohishi, Y., & Hirao, N. (2010). Compression of FeSi, Fe_3C, $Fe_{0.95}O$, and FeS under the core pressures and implication for light element in the Earth's core. *Journal of Geophysical Research*, *115*, B09204. https://doi.org/10.1029/2009JB006975

Sha, X., & Cohen, R. (2006). Lattice dynamics and thermodynamics of bcc iron under pressure: First-principles linear response study. *Physical Review B*, *73*, 104303. https://doi.org/10.1103/PhysRevB.73.104303

Siebert, J., Badro, J., Antonangeli, D., & Ryerson, F. J. (2012). Metal-silicate partitioning of Ni and Co in a deep magma ocean. *Earth and Planetary Science Letters*, *321-322*, 189–197. https://doi.org/10.1016/j.epsl.2012.01.013

Singh, A. K., Mao, H.-K., Shu, J., & Hemley, R. J. (1998). Estimation of single-crystal elastic moduli from polycrystalline X-ray diffraction at high pressure: Application to FeO and iron. *Physical Review Letters*, *80*(10), 2157–2160. https://doi.org/10.1103/PhysRevLett.80.2157

Sinogeikin, S. V., Smith, J. S., Rod, E., Lin, C., Kenney-Benson, C., & Shen, G. (2015). Online remote control systems for static and dynamic compression and decompression using diamond anvil cells. *Review of Scientific Instruments*, *86*, 72209. https://doi.org/10.1063/1.4926892

Steinle-Neumann, G., Stixrude, L., & Cohen, R. E. (1999). First-principles elastic constants for the hcp transition metals Fe, Co, and Re at high pressure. *Physical Review B*, *60*(2), 791–799. https://doi.org/10.1103/PhysRevB.60.791

Steinle-Neumann, G., Stixrude, L., Cohen, R. E., & Gülseren, O. (2001). Elasticity of iron at the temperature of the Earth's inner core. *Nature*, *413*, 57–60. https://doi.org/10.1038/35092536

Stevenson, D. J. (1977). Hydrogen in the Earth's core. *Nature*, *268*, 130–131.

Sturhahn, W. (2017). MINeral physics UTIlities (MINUTI) open source software package. www.nrixs.com

Takafuji, N., Hirose, K., Ono, S., Xu, F., Mitome, M., & Bando, Y. (2004). Segregation of core melts by permeable flow in the lower mantle. *Earth and Planetary Science Letters*, *224*(3-4), 249–257. https://doi.org/10.1016/j.epsl.2004.05.016

Takahashi, T., Bassett, W. A., & Mao, H.-K. (1968). Isothermal compression of the alloys of iron up to 300 kilobars at room temperature: Iron-nickel alloys. *Journal of Geophysical Research*, *73*(14), 4717–4725. https://doi.org/10.1029/JB073i014p04717

Tateno, S., Hirose, K., Komabayashi, T., Ozawa, H., & Ohishi, Y. (2012). The structure of Fe-Ni alloy in Earth's inner core. *Geophysical Research Letters*, *39*, L12305. https://doi.org/10.1029/2012GL052103

Tateno, S., Hirose, K., Ohishi, Y., & Tatsumi, Y. (2010). The structure of iron in Earth's inner core. *Science*, *330*(6002), 359–361. https://doi.org/10.1126/science.1194662

Tateno, S., Kuwayama, Y., Hirose, K., & Ohishi, Y. (2015). The structure of Fe-Si alloy in Earth's inner core. *Earth and Planetary Science Letters*, *418*, 11–19. https://doi.org/10.1016/j.epsl.2015.02.008

Thompson, E. C., Chidester, B. A., Fischer, R. A., Myers, G. I., Heinz, D. L., Prakapenka, V. B., & Campbell, A. J. (2016). Equation of state of pyrite to 80 GPa and 2400 K. *American Mineralogist*, *101*(5), 1046–1051. https://doi.org/10.2138/am-2016-5527

Toby, B. H., & Von Dreele, R. B. (2013). GSAS-II: The genesis of a modern open-source all purpose crystallography software package. *Journal of Applied Crystallography*, *46*, 544–549. https://doi.org/10.1107/S0021889813003531

Uchida, T., Wang, Y., Rivers, M. L., Sutton, S. R., & Gpa, K. (2001). Stability field and thermal equation of state of ϵ-iron determined by synchrotron X-ray diffraction in a multianvil apparatus. *106*(B10), 21,799–21,810. https://doi.org/10.1029/2001JB000258

Vočadlo, L., Dobson, D. P., & Wood, I. G. (2009). Ab initio calculations of the elasticity of hcp-Fe as a function of temperature at inner-core pressure. *Earth and Planetary Science Letters*, *288*(3-4), 534–538. https://doi.org/10.1016/j.epsl.2009.10.015

Weidner, D. J., Li, L., Davis, M., & Chen, J. (2004). Effect of plasticity on elastic modulus measurements. *Geophysical Research Letters*, *31*, L06621. https://doi.org/10.1029/2003GL019090

Wenk, H., Matthies, S., Hemley, R. J., Mao, H., & Shu, J. (2000). The plastic deformation of iron at pressures of the Earth's inner core. *Nature*, *405*, 1044–1047. https://doi.org/10.1038/35016558

Wenk, H. R., Takeshita, T., Jeanloz, R., & Johnson, G. C. (1988). Development of texture and elastic anisotropy during deformation of hcp metals. *Geophysical Research Letters*, *15*(1), 76–79. https://doi.org/10.1029/GL015i001p00076

Wood, B. J. (1993). Carbon in the core. *Earth and Planetary Science Letters*, *117*(3-4), 593–607. https://doi.org/10.1016/0012-821X(93)90105-I

Wood, B. J., Li, J., & Shahar, A. (2013). Carbon in the core: Its influence on the properties of core and mantle. *Reviews in Mineralogy and Geochemistry*, *75*(1), 231–250. https://doi.org/10.2138/rmg.2013.75.8

Yamazaki, D., Ito, E., Yoshino, T., Yoneda, A., Guo, X., Zhang, B., et al. (2012). P-V-T equation of state for ϵ-iron up to 80 GPa and 1900 K using the Kawai-type high pressure apparatus equipped with sintered diamond anvils. *Geophysical Research Letters*, *39*, L20308. https://doi.org/10.1029/2012GL053540

Yu, X., Zhang, J., Zhang, Y., Wang, L., & Zhao, Y. (2012). Comparative studies of yield strength and elastic compressibility between nanocrystalline and bulk cobalt. *Journal of Applied Physics*, *111*, 113506. https://doi.org/10.1063/1.4724338

Zarochentsev, E. V., Troitskaya, E. P., & Chabanenko, V. V. (2004). Elastic constants of noble-gas crystals under pressure and the Cauchy relations. *Physics of the Solid State*, *46*(2), 249–253. https://doi.org/10.1134/1.1649419

Zha, C. S., Mao, H. K., & Hemley, R. J. (2004). Elasticity of dense helium. *Physical Review B*, *70*, 174107. https://doi.org/10.1103/PhysRevB.70.174107

Zhang, J., & Guyot, F. (1999). Thermal equation of state of iron and $Fe_{0.91}Si_{0.09}$. *Physics and Chemistry of Minerals*, *26*(3), 206–211. https://doi.org/10.1007/s002690050178

Zhang, D., Jackson, J. M., Zhao, J., Sturhahn, W., Alp, E. E., Hu, M. Y., et al. (2016). Temperature of Earth's core constrained from melting of Fe and $Fe_{0.9}Ni_{0.1}$ at high pressures. *Earth and Planetary Science Letters*, *447*, 72–83. https://doi.org/10.1016/j.epsl.2016.04.026

Zhang, Y. G., & Yin, Q. Z. (2012). Carbon and other light element contents in the Earth's core based on first-principles molecular dynamics. *Proceedings of the National Academy of Sciences of the United States of America*, *109*(48), 19,579–19,583. https://doi.org/10.1073/pnas.1203826109

Zhao, J., & Ross, N. L. (2015). Non-hydrostatic behavior of KBr as a pressure medium in diamond anvil cells up to 5.63 GPa. *Journal of Physics: Condensed Matter*, *27*(18), 185402. https://doi.org/10.1088/0953-8984/27/18/185402